UNIVERSIDAD NACIONAL DE COLOMBIA

Design of a laboratory-scale reactor for the in-situ gas characterization of Fluid Catalytic Cracking (FCC)

Juan Guillermo Lacayo-Lacayo

Universidad Nacional de Colombia
Facultad de Minas, Departamento de Procesos y Energía
Medellín, Colombia
2019

Design of a laboratory-scale reactor for the in-situ gas characterization of Fluid Catalytic Cracking (FCC)

Juan Guillermo Lacayo-Lacayo

Tesis presentada como requisito parcial para optar al título de
(A dissertation presented in partial fulfilment of the requirements for the degree of):

Magister en Ingeniería Química
(Master in Chemical Engineering)

Director (Supervisor):
Alejandro Molina

Grupo de Investigación (Research group):
Bioprocesos y Flujos reactivos

Universidad Nacional de Colombia
Facultad de Minas, Departamento de Procesos y Energía
Medellín, Colombia
2019

To my family and Mary, thank you for supporting me on this journey.

Acknowledges

Professor Alejandro Molina. Departamento de Procesos y Energía. Universidad Nacional de Colombia – Sede Medellín (Medellín-Colombia).

Professor Hugo de Lasa. Department of Chemical and Biochemical Engineering. Western University (London-Canada).

Grupo de investigación Bioprocesos y Flujos Reactivos. Departamento de Procesos y Energía. Universidad Nacional de Colombia – Sede Medellín (Medellín-Colombia).

Colciencias-Ecopetrol (Contract no. 0423 2013).

Emerging Leaders in the Americas (ELAP) Canadian Exchange Program.

Western University (London-Canada).

Abstract

A laboratory-scale reactor was designed and built to test optical techniques for the online and in situ monitoring of the fluid catalytic cracking (FCC) reaction progress. A one-dimensional and a three-dimensional computational fluid dynamics (CFD) model, were proposed and solved to assist in the design and to understand the hydrodynamic, mixing, heat and mass transfer phenomena taking place in the reactor. The reactor setup included Evaporation, Heating, Reaction, and Separation zones to evaporate the liquid feed, heat the catalyst particles, allow for the reaction and separate the catalyst from the gaseous stream, respectively. The reactor was a fused-quartz cylinder, 180 cm long and with an internal diameter of 1.3 cm. Five electrical furnaces that could be displaced in the vertical direction provided the heat required to maintain the gas temperature flowing in the reactor at a nominal value while provided space for passing the laser beam through the reactor to characterize the system. A mid-infrared He-Ne laser operating at 3.39 μm wavelength was used to evaluate the concentration of 1-hexene, that was selected as a model compound to represent FCC reactions. Experiments at different temperatures (373 K to 673 K) and 1-hexene concentrations (2.5 mol/m^3 to 12.5 mol/m^3), in the presence and absence of equilibrated FCC catalyst, demonstrated that the fractional transmission presents a linear response to 1-hexene concentration. Despite the fact that the optical setup did not incorporate an on-site correction for laser drift, the results are highly encouraging and suggest that inference of the advance of the FCC reaction with optical techniques in FCC systems of larger scale is possible.

Keywords: Fluid catalytic cracking, downer reactor, mid-infrared, in situ measurement.

Resumen

Se diseñó y construyó un reactor a escala laboratorio para probar técnicas ópticas de monitoreo en línea e in situ del avance de reacción de craqueo catalítico fluidizado (FCC, por sus siglas en inglés). Fueron propuestos y resueltos un modelo en una dimensión y un modelo de tres dimensiones en dinámica de fluidos computacional (CFD, por sus siglas en inglés) los cuales se tomaron como base para el diseño y comprensión de los fenómenos hidrodinámicos, de mezcla y de transferencia de calor y masa que toman lugar en el reactor. La configuración del reactor incluyó zonas de evaporación, calentamiento, reacción y separación para evaporar la alimentación líquida, calentar las partículas de catalizador, permitir la reacción y separar el catalizador de la corriente gaseosa, respectivamente. El reactor fue un cilindro de cuarzo fundido de 180 cm de largo y con un diámetro interno de 1.3 cm. Cinco hornos eléctricos con capacidad de moverse verticalmente proporcionaron el calor necesario para mantener la temperatura del gas que fluye en el reactor a un valor nominal, además, se habilitó un espacio para que el rayo láser pudiese pasar a través del reactor y así caracterizar el sistema. Se usó un láser He-Ne en el infrarrojo medio que funcionaba a una longitud de onda de 3.39 μm para evaluar la concentración de 1-hexeno, que se seleccionó como compuesto modelo para representar las reacciones de FCC. Experimentos a diferentes temperaturas (373 K hasta 673 K) y concentraciones de 1-hexeno (2.5 mol/m^3 a 12.5 mol/m^3), con presencia y ausencia de catalizador de FCC en equilibrio, demostraron que la absorción fraccional presenta una respuesta lineal a la concentración de 1-hexeno. Aunque el montaje óptico no incorporó una corrección en el sitio para la desviación de voltaje del láser, los resultados son altamente alentadores y sugieren que es posible inferir el avance de la reacción FCC con técnicas ópticas en sistemas de FCC a mayor escala.

Palabras claves: Craqueo catalítico fluidizado, reactor de lecho transportado descendente, infrarrojo medio, medición in situ.

Content

Acknowledges vii

Abstract ix

Resumen x

List of figures xiii

List of tables xv

Introduction 1

1 Fundamentals of Fluid catalytic cracking (FCC) and laboratory-scale approximation units 3

- 1.1 Fluid catalytic cracking (FCC) . . . 3
  - 1.1.1 FCC unit . . . 3
  - 1.1.2 Reactor configuration . . . 3
  - 1.1.3 FCC catalysts . . . 4
  - 1.1.4 FCC reactions . . . 5
- 1.2 Laboratory-scale approximation units . . . 6
- 1.3 Optical techniques in FCC research . . . 7
- 1.4 Concluding remarks . . . 8

2 A lab-scale reactor for the in-situ gas characterization of a Fluid Catalytic Cracking (FCC) reaction 9

- 2.1 Abstract . . . 9
- 2.2 Introduction . . . 9
- 2.3 Model . . . 10
  - 2.3.1 1-D model . . . 11
  - 2.3.2 CFD simulation . . . 17
- 2.4 Experimental section . . . 20
  - 2.4.1 Optical setup . . . 22
- 2.5 Results . . . 23
  - 2.5.1 Simulation . . . 23
  - 2.5.2 Optical measurements . . . 28

2.6 Conclusions 30

3 Conclusions and future work 38

3.1 Conclusions 38
3.2 Future work 38

List of figures

1-1 General scheme of a FCC riser unit [1]. 4
1-2 Lab-scale FCC reactors classification from the point of view of catalyst bed and gas flow pattern [21]. 6

2-1 Schematics that represents the FCC process. 11
2-2 Differential volume in the particle heating zone. 12
2-3 Reaction scheme that represents the catalytic cracking of TIPB [27]. 16
2-4 Validation of the reaction mechanism used in the simulation. Comparison of model predictions with kinetic data. Symbols: experimental data. Lines: model predictions. 17
2-5 Lateral views of the mesh for the top of the reaction zone. 19
2-6 Experimental aparatus 1) Evaporation zone, 2) Particle heating zone, 3) Reaction zone, 4) Separation zone. 21
2-7 Photo of the optical setup adapted to the reactor. 1) He-Ne Laser, 2) Optical chopper and 3) Photodetector. 22
2-8 Temperature profile along the heating zone. Results are for simulations results of the 1D and CFD simulations and from the experiments. Error bars represent one standard deviation. 24
2-9 Gas velocity profile along the reactor as predicted by the 1D and the CFD simulations. 25
2-10 Particle velocity profile along the reactor as predicted by 1D and CFD simulations. 26
2-11 Predicted global conversion by the 1D and CFD simulations. 27
2-12 Comparison of the temperature profile along the reactor as predicted by the CFD model and as measured in the experiments. Error bars represent one standard deviation. 27
2-13 Variation of the fractional transmission (I/I_0) with the molar fraction of 1-hexene at different temperatures and in the presence and absence of catalyst. 29
2-14 Fractional transmission at different 1-hexene concentrations. 29
2-15 Variation of temperature with time in the Reactant evaporation zone. 31
2-16 Calibration curve for the volumetric screw feeder. 31
2-17 Actual setup picture and the four zones considered. 32

2-18 Variation in laser intensity with time. Only the chopper was between the laser and the detector. 33
2-19 Typical behavior of voltage in time for an experiment with catalyst and 1-hexene. 34
2-20 Velocity vectors colored by Y velocity in the region were the feed (entering from both sides at the top of the figure) and catalyst and nitrogen mix. . . . 36
2-21 Velocity vectors colored by temperature. 37
2-22 Variation of laser intensity when fresh catalyst (0 s - 300 s) and 1-pass catalyst (300 s - 850 s) enter a flow of 1-hexene at atmospheric temperature. 37

List of tables

2-1 Coefficients to compute the nitrogen physical properties [54]. 19
2-2 Models used in the CFD simulation. 20
2-3 Data obtained from Figure **2-19**. 35

Introduction

Fluid Catalytic Cracking (FCC) units are of paramount importance in the oil refinery process, in these units, heavy gas oil is converted into lighter products with higher added value, mainly gasoline. It is estimated that approximately 50% of the installed capacity for the major conversion processes in refineries is contributed by FCC [1]. In the last years, while fuel demand is increasing, unconventional feeds with a large number of impurities are becoming more common. Dealing with these new challenges demands not only new and more robust catalysts but also process improvements [2].

Traditionally [3, 4, 5], analytical techniques, such as gas chromatography (GC), mass spectrometry (MS) or the combination of both (GC-MS), have been used to measure the aromatic and saturate contents of the FCC streams to determine the process global conversion. The complete time required to establish conversion with these techniques may be more than 10 minutes, while the FCC reactions only take from 2 to 10 seconds [6].

The quality of a product obtained in a reactive process depends, in part, on the ability to measure, monitor and control the process variables in a time scale similar to that of the process. The development of online measurement techniques brings significant benefits that extend to product quality, staffing needs and other areas that affect the overall economy of a plant. Optical techniques are considered a good option for gas sensing. Nevertheless, its application to FCC has been scarce. Recently, however, López et al.[7] documented the viability of monitoring the progress of catalytic cracking for model compounds in the MIR (3200–2800 cm^{-1}) range. In their analysis, Lopez et al. used catalyst-free streams.

Application of the methodology described by López et al. to actual in situ detection of the advance of the FCC reaction would demand the ability to deal with the possible interference of the catalyst particles. Different laboratory-scale reactors and design configurations have been typically used for kinetics and catalyst evaluation, and for hydrodynamics studies of the process as well [8, 9, 10, 11]. None have implemented optical analysis and, as far as the author knows, cannot be used to evaluate the effect of particles on the optical setup described in Ref [7].

The main objective of this research is to design a laboratory-scale gas-solid reactor for the in situ characterization of the advance of reaction in Fluid Catalytic Cracking (FCC). It considers two specific objectives: To define the lab-scale reactor dimensions and operating conditions and, to validate the operation of the reactor for the in-situ characterization of the reactions in FCC.

This dissertation has three chapters. Chapter 1 deals with FCC fundamentals and gives a review on current laboratory-scale setups for the characterization of FCC processes. Chapter 2, written as a freestanding manuscript, follows the traditional format of a journal paper. Chapter 2 focuses on the general design of the laboratory-scale unit, from conceptual design to a three-dimensional CFD simulation. It also describes the construction of the reactor, the optical setup used for the experiments, and the evaluation of this optical setup in the reactor. Chapter 3 presents conclusions and recommendations for future research.

1 Fundamentals of Fluid catalytic cracking (FCC) and laboratory-scale approximation units

This chapter describes the FCC process and the state of the art of the laboratory-scale FCC units.

1.1 Fluid catalytic cracking (FCC)

FCC is a crude oil refining process where heavier fractions are upgraded to lighter fractions with more relevance on the market, making it a key process nowadays as the global demand for transportation fuels is growing.

1.1.1 FCC unit

A general scheme of an FCC unit is presented in Figure **1-1**. An FCC unit includes three principal sections: reactor, stripper, and regenerator. The catalytic process is carried out in the reactor. The feed, normally gas oil at $473 - 673\ K$, makes contact with the solid preheated catalyst ($950 - 1000\ K$), commonly zeolite, at the entrance of the reactor and the difference in temperatures causes the vaporization of the feed [6]. The feed reacts at the catalyst surface and produces lighter components. The ratio of catalyst to oil (CTO) is one of the variables to manipulate in the process. At the exit of the reactor, the product stream is separated from the spent catalyst in a series of cyclones (stripper). The spent catalyst, deactivated by the deposition of carbonaceous material (coke) on its surface, is injected into the regenerator in which hot air burns the deposited coke. The regenerated catalyst goes to the reactor and thus, the cycle begins again. To maintain the desired catalyst activity, fresh catalyst is continually added to the unit and replaces a fraction of equilibrated catalyst that is constantly removed.

1.1.2 Reactor configuration

Since the first FCC units, in the early 40s [12], reactors in which the reactant and catalyst enter by the bottom and flow upward have traditionally been used, these reactors are known

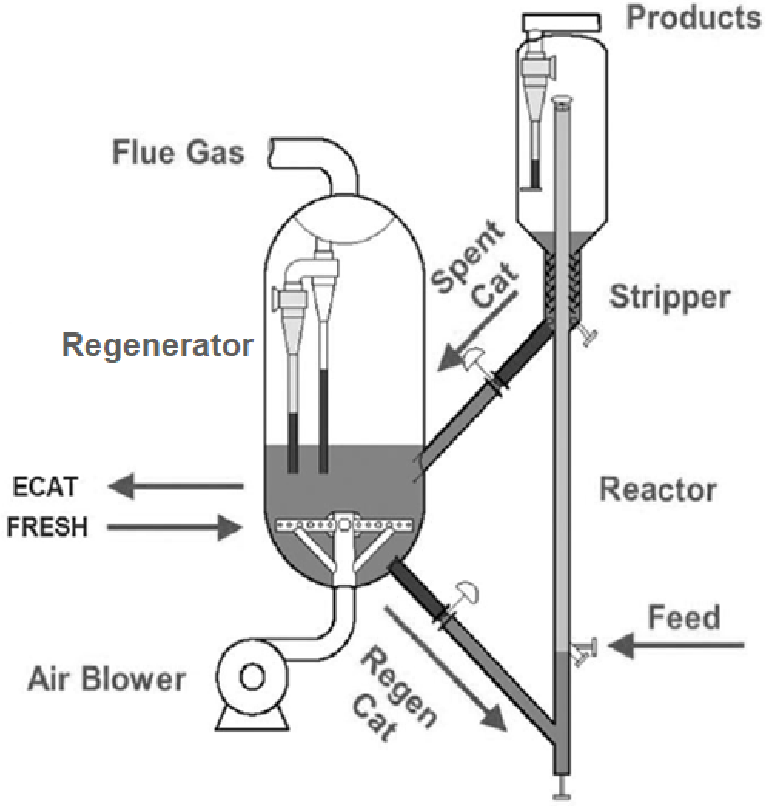

Figure 1-1: General scheme of a FCC riser unit [1].

as *risers*. Figure **1-1**, for instance, represents this configuration; note that the stripper is on the top of the reactor. To improve performance, *downer* reactors have been proposed. In these, the reactant and the catalyst enter from the top and flow downward [13]. The main differences between the performance of both configurations are closely related to hydrodynamics. The riser configuration experience solid backmixing because both gas and solids flow against gravity. This reduces the efficiency of gas-solid contact and leads to an undesired distribution of products due to reduced selectivity [14]. Particles accelerate faster in the downer configuration because of the gravity force. This effect causes a more uniform radial distribution so that near plug flow behavior is obtained [15].

1.1.3 FCC catalysts

Current FCC catalysts are in the form of fine powders with a typical particle size of 75 μm and have three major components: the active component, the matrix, and functional ingredients [16]. The active component is usually zeolite, and it is responsible for most of the catalyst activity. Zeolite has a well-known crystal structure formed by tetrahedral structures in which a silicon or aluminum atom is at the center of the tetrahedron, with oxygen atoms at the four corners. There are two types of zeolites commonly used in FCC: type X and type

Y. The silica/alumina ratio is lower in type X, of the order of 2. The second component is the matrix, composed of substances different than the zeolite but that could have certain catalytic activity. Normally the matrix is alumina [17] and provides the primary cracking sites. Finally, the functional components are those that perform a specific function, for instance, to bind the catalyst components or to catch heavy metals from the feed.

Depending on the state of the catalyst it can be classified as fresh catalyst, spent catalyst and equilibrated catalyst (E-cat). When fresh catalyst takes part in a reaction it becomes spent catalyst due to coke formation in its surface. When the coke is burned in a regenerator it turns into equilibrated catalyst.

To evaluate the performance of a catalyst, laboratory standard tests are used (see Section 1.2), commonly, three important performance characteristics are measured: conversion and the coke and gas formation [6]. Surface area, bulk density, pore volume, pore diameter, and particle size distribution are important physical properties of a catalyst, that are even considered for FCC design decisions.

1.1.4 FCC reactions

Cracking reactions require contact times, or time on stream (TOS), that are short, between two to ten seconds. Because of these short times, most cracking in the FCC process is catalytic. Nevertheless, thermal cracking also occurs when the feed is exposed to high temperature (700 - 925 K) in the absence of a catalyst and its magnitude depends on time and temperature [18]. Product distribution is different for both kinds of cracking reactions [19] as these two processes follow different reaction mechanisms. Improvements in reactor mixing and separation of cracked products are actions that can minimize thermal cracking.

Generally, catalytic cracking reactions could be divided into two groups: primary cracking and rearrangement-recracking reactions. Moreover, one could be more specific and define three main types of reactions: cracking of C-C bond, isomerization, and hydrogen transfer. The first one consists of the splitting of the C-C bonds and it normally takes place in long-chain hydrocarbons as they are more reactive than short-chain hydrocarbons. Isomerization refers to molecule rearrangement into more stable molecules (with same molecular weight) and is linked to a high octane number. The third one consists of hydrogen transfer between olefins to form paraffins and then aromatics. It is important to mention another important reaction that plays a key role in the process, coking. Coke, is an undesirable product in FCC and the mechanism for its formation is not very clear, but it is believed that reactions producing unsaturates and multiring aromatics are the principal coke-forming compounds [20].

1.2 Laboratory-scale approximation units

Figure **1-2** shows [21] the different laboratory approximations for FCC units, from the point of view of catalyst bed and gas flow pattern. Corma & Sauvanaud [21] report improvements in laboratory FCC testing for reactor configurations closer to the right in Figure **1-2** as they capture more phenomena involved in the actual process. The differences between them are discussed below.

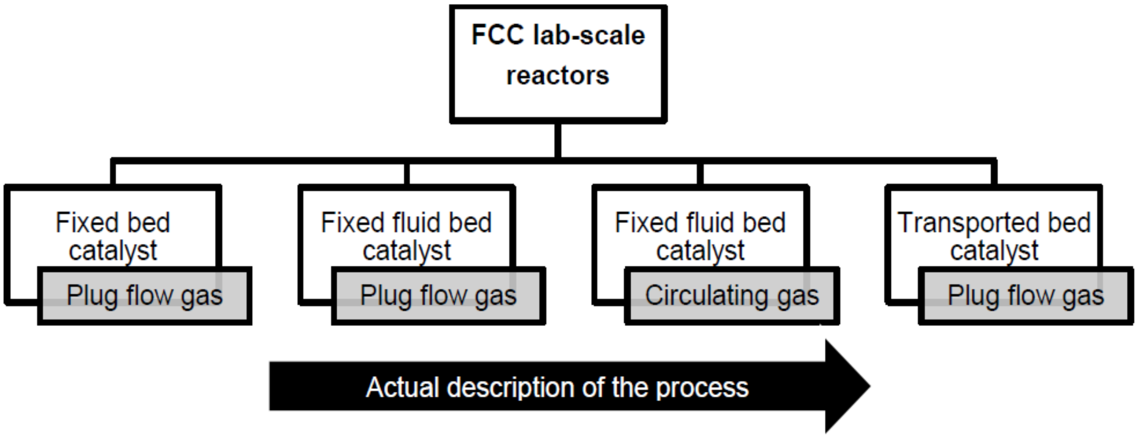

Figure 1-2: Lab-scale FCC reactors classification from the point of view of catalyst bed and gas flow pattern [21].

From the '80s, laboratory-scale configurations have been proposed to evaluate possible improvements to the process, mostly to address the performance of new catalysts. To create a piece of equipment that could be used to compare and select a catalyst between the large commercial offer, a standard test (ASTM D3907) [22], the Micro Activity Test (MAT), was conceived. The MAT consists of a fixed bed reactor where the catalyst sample (4 grams) is packed in a quartz-tube section and a pulse of feed (1 – 1.5 grams) is injected during a specific period of time (75 seconds). Despite being a good catalysts-comparison tool, it is evident that the set of conditions for this test does not represent the conditions at industrial scale. For instance, it is not a transported bed and the TOS between the gas and catalyst is over 20 times greater than the actual value. Accordingly, in the literature, a large number of modified MAT configurations with different conditions have been reported [23, 24, 25, 26]. Fixed bed catalytic reactors, such as MAT, were the starting point for catalytic fixed fluid bed reactors. In these, the catalyst bed is fluidized, which eliminates the formation of temperature profile and coke profile along the bed and modifies hydrodynamics [8]. Looking for improvements that reduce the hydrodynamics differences, a recycle reactor, called Riser Simulator®, was designed by de Lasa [9]. This equipment consists of a 45 mL confined reactor that comprises an upflow zone and a downflow zone. On the top, an impeller makes the gas circulate. In the upflow zone a basket holds the catalyst, which flows faster than the fluidization velocity but lower than the drift velocity. The external annular space is the downflow zone. In the Riser Simulator®, TOS are between 3 – 10 seconds and temperatures, pressures, and CTO are similar to those of the actual FCC unit. Besides catalyst evaluation, this reactor has been used for the study of reaction kinetics of light gas oil [27] and biomass gasification [28].

The approximations above were mainly conceived for evaluating catalysts performance and are slightly distant from the actual FCC unit. Trying to minimize the gap between laboratory-scale and actual units, transported bed reactors have been developed. In these, the contact between phases is more representative of the FCC industrial reactors. The Microriser® [10] unit is one of them. This reactor can be operated in an ideal plug-flow regime, it is isothermal, and the residence time can be varied by changing the reactor length (by adding or removing sections), without changing the catalyst and feedstock flow rates [29]. Due to the above, the reactor can be easily modeled through a plug flow, isothermal model, which facilitates kinetic data extraction. To circulate the catalyst in the reactor, gas (typically nitrogen) entrainment is needed. The geometry of the reactor allows that temperature and contact time can be well controlled. Some examples of kinetic studies on this reactor are those conducted with aromatic feeds [30] and naphtha cracking [31].

Another relevant transported bed reactor with plug flow for FCC study is the Microdowner®. The advantage of this unit over traditional laboratory processes, such as MAT and its modifications, is that it achieves a very short residence time of the solid in the reactor that is truly representative of the industrial process. The Microdowner® unit consists of a tube of constant circular section (9 *mm*). In a similar way to the Microriser® unit, the length can be modified by attaching new sections of pipe to the existing reactor, two sections of reactor 50 *cm* long are normally used to form a reactor total length of 50 or 100 *cm* depending on the desired residence time [11]. While all these lab-scale reactors present advantages and disadvantages for the study of the FCC process, they all have in common that the analysis of the feed conversion is carried out downstream of the reactor. Furthermore, none of them consider optical access for the optical diagnostics methods.

1.3 Optical techniques in FCC research

The use of optical techniques for FCC investigation has been closely related with the development of optical-fiber probes for particle velocity and cluster sizing measurements at atmospheric conditions [32, 33, 34, 35]. However, recently, a laser technique for monitoring the progress of catalytic cracking reaction have been proposed by Lopez-Zamora et al. [7]. Using Mid-Infrared (MIR) spectroscopy Lopez-Zamora et al. proposed a methodology to evaluate the global conversion based on the kind of C-H bonds present in hydrocarbons and the Beer-Lambert's law. The experiments were conducted with a helium-neon (HeNe) laser, operating at 2949.85 cm^{-1} wavenumber (3.39 μm wavelength) using 1-hexene and 1,3,5-triisopropyl benzene (TIPB) as model compounds. The Riser Simulator® operating at 823 K, CTO = 2.5 and TOS = 7 sec was used to validate the method, a fiber optic sensor was employed to locate the laser beam aiming at the external annular space (downflow zone) of the reactor, without the presence of particles. In the refereed literature no other optical diagnostic method was applied for the characterization of the FCC reaction.

1.4 Concluding remarks

There had been significant advances in the laboratory-scale analysis of FCC systems. There is, however, still range form improvement. One is the fact that to determine the global conversion of the process, gas products need to be sampled downstream and concentration needs to be measured with analytical techniques (mainly GC) that take more than one order of magnitude longer to give an answer that the total duration of the FCC experiments. This is the case for commercial and laboratory-scale applications.

Nevertheless, laser techniques have been documented as having the potential for in situ monitoring the progress of the FCC reaction. The current development of this technique does not document the effect of particles in the system. This thesis aims to develop a lab-scale setup that closes this gap, i.e. that can be used to characterize, in situ, the progress of the FCC reaction.

2 A lab-scale reactor for the in-situ gas characterization of a Fluid Catalytic Cracking (FCC) reaction

2.1 Abstract

Evidence that a helium-neon (He-Ne) laser operating in the Mid-infrared (MIR) at a wavelength of 3.39 μm can detect variations of 1-hexene concentration in the presence of catalyst at conditions relevant for FCC is provided. The in situ and online characterization of catalytic cracking (FCC) reactions is important to improve process control and boost efficiency. In this research, a laboratory-scale downer unit was design and built. One-dimensional and Computational Fluid Dynamics (CFD) simulations aimed at helping the design and improving the understanding of the mixing and hydrodynamics of the system were conducted. The lab-scale reactor was 180 cm long, had an internal diameter of 1.3 cm, and was made of fused quartz to allow the passage of the laser beam. A surrogate of a FCC feed, 1-hexene, was carefully metered, vaporized, and fed into the reactor through two inputs located at an angle of 45 degrees from the vertical descendent flow and 70 cm below the input of an equilibrated FCC catalyst (0.5 g/s) and a flow of 0.55 $slpm$ of purge and entraining N_2. A system of five heaters, that can be displaced in the vertical direction to allow the passage of the laser beam, guaranteed temperatures up to 923 K. The system can continuously operate for up to 1 hour. The experimental results show a linear response of fractional transmission with the 1-hexene concentration that was independent of temperature in the 373 K to 673 K range in a span of concentrations that was much higher than that used in other FCC characterization equipment. The experimental setup allowed to demonstrate the ability of the laser system to measure the 1-hexene concentration even in the presence of catalyst.

Keywords: Fluid catalytic cracking, Downer reactor, HeNe laser, In situ measurements.

2.2 Introduction

Fluid Catalytic Cracking (FCC) units are of paramount importance in the oil refinery process. In these units, heavy gas oil is converted into lighter products with higher added-value.

It is estimated that approximately 50% of the installed capacity for the major conversion processes in refineries is contributed by FCC [1], and the process accounts for about 35–50% of the total gasoline produced worldwide in the petroleum industry [36]. Traditionally, analytical techniques such as gas chromatography (GC), mass spectrometry (MS) or the combination of both (GC-MS) have been used to measure the aromatic and saturate contents of the FCC exit streams and to determinate the process global conversion. Interestingly, the analysis in these techniques takes more than 10 minutes, while the FCC reactions take 3 seconds or less [6]. The development of measurement techniques that operate in situ and give real-time information may be beneficial for the study of the chemical processes taking place during FCC and their interactions with the complex hydrodynamics taking place in circulating fluidized beds. Real-time information may be also useful for process control.

Optical techniques are considered a good option for online and in situ gas sensing. In FCC, there is an important history of the use of optical-fiber probes for particle velocity and cluster sizing measurements at atmospheric conditions [34, 32, 35]. However, in the refereed literature, only Lopez-Zamora et al. [7] have documented the use of optical analysis to characterize the FCC reaction. Using Mid-Infrared (MIR) spectroscopy Lopez-Zamora et al. proposed a methodology to evaluate the global conversion based on the kind of C-H bonds present in hydrocarbons and the Beer-Lambert's law. The experiments were conducted with a helium-neon (HeNe) laser, operating at 2949.85 cm^{-1} wavenumber (3.39 μm wavelength) using 1-hexene and 1,3,5-triisopropyl benzene (TIPB) as model compounds. The Riser Simulator® operating at 823 K, CTO = 2.5 and TOS = 7 *sec* was used to validate the method, a fiber optic sensor was employed to locate the laser beam aiming at the external annular space (downflow zone) of the reactor, without the presence of particles. In the refereed literature no other optical diagnostic method was applied for the characterization of the FCC reaction. The evaluation of the effect of catalyst particles on the ability of the MIR described in Ref. [7] is an important step towards the widespread application of this technique for the characterization of FCC systems.

While different laboratory-scale reactors have been widely used for kinetic and catalysts evaluation [9, 10, 11], in their original configurations it is difficult to couple an optical setup to perform in situ and in real time measurements in the presence of a catalyst. We report the design and construction of such a setup. The equipment was conceived as a testing tool for optical techniques and allows a wide range of operating conditions.

2.3 Model

Figure **2-1** presents a sketch of the downer setup. The catalyst is preheated and mixed with the reactant; the reaction follows while both phases are flowing downwards. Finally, products and spent catalyst are separated. Actual FCC units involve a regenerator to burn the coke deposited on the catalyst surface. The setup designed in this thesis does not recycle the catalyst, therefore, it does not include a regenerator. The design of the setup was assisted by calculations carried out with two models: a one-dimensional model that simplifies the hydrodynamics as plug flow that was mainly oriented at understanding the chemical reactions; and a three-dimensional CFD simulation that made emphasis in heat transfer and mixing. Both models consider a particle heating zone and a reaction zone which have been simulated separately.

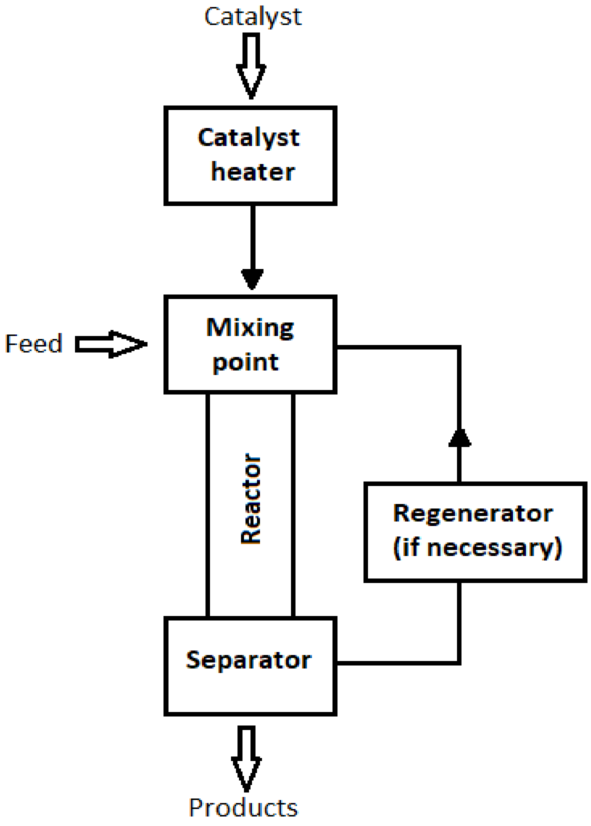

Figure 2-1: Schematics that represents the FCC process.

2.3.1 1-D model

Equation (2-1) presents the balance of the forces acting on a catalyst particle and that it is used to predict the particle trajectory in the reactor.

$$F_T = m_p \cdot \frac{dU_p}{dt} = m_p \cdot g + F_D + F_B \tag{2-1}$$

In equation (2-1), F_T is the total force acting on the particle, m_p is the particle mass, U_p is the particle velocity, F_D is the drag force, F_B is the buoyancy force, and g is the acceleration due to gravity. Both sides of the equation can be divided and multiplied by m_p and dt/dz respectively:

$$m_p \cdot \frac{dU_p}{dt} \cdot \frac{1}{m_p} \cdot \frac{dt}{dz} = (m_p \cdot g + F_D + F_B) \cdot \frac{1}{m_p} \cdot \frac{dt}{dz} \tag{2-2}$$

Reorganizing,

$$\frac{dU_p}{dz} = \frac{g + \frac{F_D}{m_p} + \frac{F_B}{m_p}}{U_p} \tag{2-3}$$

Equation (2-3) describes the change in particle velocity along the reactor. The drag and buoyancy forces were defined as follows:

$$F_D = \frac{1}{2} \cdot \rho_g \cdot (U_p - U_g) \cdot |U_p - U_g| \cdot C_D \cdot A_{pro} \cdot (1 - \varepsilon)^{-2.65} \tag{2-4}$$

$$F_B = \rho_g \cdot V_p \cdot g \tag{2-5}$$

where, ρ_g is the gas density, U_g is the gas velocity, C_D is drag coefficient, A_{pro} is the particle projected area and V_p is the particle volume. The expression $(1-\varepsilon)^{-2.65}$ is a correction when a large number of particles is considered [37]. Morsi-Alexander's correlation for the drag coefficient [38] was selected for this research because it proposes a more complete approach as particle Reynolds (Re_p) domain is divided into eight successive Re_p ranges by means of adjusting eight corresponding fits.

The energy balance for the differential volume in Figure **2-2** considers the steady state downward flow of gas and particles through a cylinder with a constant-temperature wall (T_w), in this way, the aim of this balance is to find the required minimum length to heat the particles up to T_w.

The ratio between the volume occupied by the gas and the cylinder volume is the void fraction (ε). This term, in a fluidized bed process like the one in this study, changes along the reactor as the particle velocity is also changing. (see Eq. (2-3)).

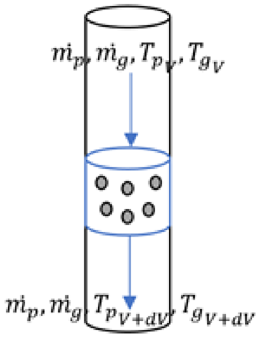
$\dot{m}_p, \dot{m}_g, T_{p_V}, T_{g_V}$
$\dot{m}_p, \dot{m}_g, T_{p_{V+dV}}, T_{g_{V+dV}}$

Figure 2-2: Differential volume in the particle heating zone.

$$\varepsilon = 1 - \frac{\dot{m}_p}{\rho_p \cdot \Omega \cdot U_p} \tag{2-6}$$

where, $\dot{m}_p$ is particle mass flow, ρ_p is the particle (catalyst) density and Ω is the cylinder cross sectional area.

The energy balance, Eq.(2-7), for the catalyst particle considers convection and radiation from the gas and wall, respectively.

$$(\dot{m}_p \cdot H_V) - (\dot{m}_p \cdot H_{V+dV}) = h_{g\to p} \cdot N \cdot A_{s_p} \cdot (T_g - T_p) + \epsilon_w \cdot \sigma \cdot (T_w^4 - T_p^4) \cdot N \cdot A_{s_p} \tag{2-7}$$

As the process does not have significantly pressure changes, the enthalpy change could be represented by $\Delta H = C_{p_p} \cdot \Delta T$, whit constant C_{p_p}. A simplified version of the energy balance for the catalyst particles is that in Eq. (2-8).

$$\dot{m}_p \cdot C_{p_p} \cdot (T_{p_V} - T_{p_{V+dV}}) = N \cdot A_{s_p} \cdot (h_{g\to p} \cdot (T_g - T_p) + \epsilon_w \cdot \sigma \cdot (T_w^4 - T_p^4)) \tag{2-8}$$

In equations (2-7) and (2-8), H is the enthalpy, $h_{g\to p}$ is the convective heat transfer coefficient from gas to particle, N is number of particles in the differential volume, A_{s_p} is particle surface area, T_g is the gas temperature, ϵ_w is wall emissivity factor, σ is the Stefan-Boltzmann constant and C_{p_p} is the particle specific heat capacity. Eq. (2-9) was used to compute the number of particles in the differential volume.

$$N = \frac{dV \cdot (1 - \varepsilon)}{V_p} \tag{2-9}$$

Combining equations (2-8) and (2-9), dividing by dV and taking limit when dV approaches zero yields the final expression for the energy balance equation, Eq. (2-10).

$$\frac{dT_p}{dz} = \frac{(1 - \varepsilon) \cdot A_{s_p} \cdot \Omega}{V_p \cdot \dot{m}_p \cdot C_{p_p}} \cdot (h_{g\to p} \cdot (T_g - T_p) + \epsilon_w \cdot \sigma \cdot (T_w^4 - T_p^4)) \tag{2-10}$$

Eq. (2-10) describes the particle temperature change in a specific length because of the convection and radiation from the gas and wall, respectively. The convective heat transfer coefficient from gas to particle $h_{g\to p}$ was calculated with the Kunii-Levenspiel correlation for Nu_p [39] as it describes the gas-solid heat transfer for a sphere surrounded by a fluid, based on physical and chemical phenomena occurring in fluidized beds.

$$Nu_p = 2 + (0.6 \cdot Re_p^{1/2} \cdot Pr^{1/3}) \tag{2-11}$$

Where, Nu_p is the Nusselt number of a particle immersed in a fluid, Re_p is the particle Reynolds number and Pr is the gas Prandtl number. In Eq. (2-12) k_g is the gas thermal conductivity and d_p is the particle diameter.

$$h_{g\to p} = \frac{Nu_p \cdot k_g}{d_p} \tag{2-12}$$

The gas energy balance, Eq. (2-13) also considered convective heat transfer from the wall and convective heat transfer to the particles.

$$\dot{m}_g \cdot C_{p_g} \cdot (T_{g_V} - T_{g_{V+dV}}) = h_{w \to g} \cdot A_w \cdot (T_w - T_g) - h_{g \to p} \cdot N \cdot A_{s_p} \cdot (T_g - T_p) \tag{2-13}$$

where, $\dot{m}_g$ is the gas mass flow, C_{p_g} is the gas specific heat capacity, $h_{w \to g}$ is the convective heat transfer coefficient from wall to gas and A_w is the wall heat transfer area, as calculated in Eq. (2-14).

$$A_w = a \cdot dV = \frac{4}{D} \cdot dV \tag{2-14}$$

where, a is the heat exchange area per unit volume and D the cylinder diameter. Using Eq. (2-9) and Eq. (2-14), dividing by dV and taking limit when dV approaches zero one obtains the final expression for the energy balance for the gas, Eq. (2-15).

$$\frac{dT_g}{dz} = \frac{\Omega}{\dot{m}_g \cdot C_{p_g}} \cdot \left(h_{w \to g} \cdot a \cdot (T_w - T_g) - h_{g \to p} \cdot \frac{(1-\varepsilon) \cdot A_{s_p}}{V_p} \cdot (T_g - T_p)\right) \tag{2-15}$$

Eq. (2-15) describes the gas temperature change because of convective heat transfer from the wall and to the particles. The convective heat transfer coefficient from wall to gas, $h_{w \to g}$, was estimated from the Nusselt number for fluid in a circular tube, which in a laminar regime and fully developed flow is 3.66 [40].

Eq. (2-3), (2-10) and (2-15) are coupled ordinary differential equations and were solved using MatLab for the particle heating zone 1D simulation. For the gas, nitrogen (N_2) has been used and its density is calculated as an ideal gas, aditionally, the gas thermal conductivity (k_g), the gas specific heat (C_{p_g}), and the gas dynamic viscosity (μ_g) have been calculated using polynomial approximations as functions of gas temperature (see Table **2-1**). Prandtl number was 0.7327, it corresponds to nitrogen at 873 K. For the catalyst, a mean diameter of 8.46×10^{-5} m, a catalyst density of 1525 kg/m^3 and particle specific heat capacity of 1090 $J/kg \cdot K$ [41] were considered. The particle density (ρ_p) value is similar to the used in other studies [42, 43] and a particle size distribution analysis was made in a Mastersizer 2000 of Malvern Instruments to obtain the mean particle diameter (d_p). A fused quartz cylinder of 0.45 m long with an internal diameter of 0.013 m and wall emissivity (ϵ_w) of 0.6 was used. The wall emissivity corresponds to that of fused quartz of 3 mm width at 800 - 900 K [44].

Nitrogen and catalyst flow of 1.00×10^{-6} kg/s and 5.00×10^{-4} kg/s were used, respectively. Both phases entered at 300 K and the cylinder wall temperature (T_w) was set at 873 K. Operation was considered at atmospheric pressure (85113 Pa for Medellin).

For reaction zone, the species conservation balance, Eq. (2-16), considered a differential volume in a steady state for a downer reactor.

$$F_i(z) - F_i(z + dz) - \Sigma r_i \cdot dz \cdot \Omega \cdot (1 - \varepsilon) \cdot \rho_p \cdot \phi = 0 \tag{2-16}$$

Dividing by dz and taking limit when dz approaches zero, Eq. (2-16) becomes Eq. (2-17).

$$\frac{dF_i}{dz} = \Sigma r_i \cdot \Omega \cdot (1 - \varepsilon) \cdot \rho_p \cdot \phi \tag{2-17}$$

where, F_i is molar flow of component i (TIPB), r_i is the reaction rate of component i (TIPB) and ϕ is the catalyst deactivation function, Eq. (2-18)[45].

$$\phi = exp \cdot [-\beta \cdot (1 - y_{TIPB})] \tag{2-18}$$

where, β is a constant equal to 5.04 and y_{TIPB} is the mass fraction of TIPB. Eq. (2-17) describes the molar flow of TIPB throughout the length of the reaction zone and is solved simultaneously with Eq. (2-3). As described below, the species balance equation was only applied to a region of the reactor where isothermal flow could be assumed. Therefore, Eq. (2-17) was solely solved in that region.

Catalyst properties have been previously mentioned, gas (N_2 and TIPB) density was calculated as an ideal gas and the gas dynamic viscosity was calculated by a mixing law. Nitrogen and catalyst flow were the same mentioned above, for TIPB a flow of 3.33×10^{-5} kg/s was used, hence, a catalyst to oil ratio (CTO) of 15. In this case, fused quartz cylinder of 1.10 m long with the same internal diameter was considered. Reaction zone operates at atmospheric pressure and 823 K.

Reaction mechanism

Laboratory-scale FCC studies simplify the complex VGO distillate fraction in a refinery, the typical feedstock of FCC unit, with less complex compounds [46, 47]. This study considers two surrogates for VGO: 1,3,5-tri-isopropylbenzene (TIPB, $C_{15}H_{24}$) with a molecular weight of 204.4 g/mol and boiling point of 507 K and 1-hexene (C_6H_{12}), with a molecular weight of 84.16 g/mol and boiling point of 336 K.

While the design of the experimental system considered TIPB, experiments were conducted with 1-hexene as the latter is easier to handle in an experimental setup given its lower boiling point. Furthermore, López [48] demonstrated that the analysis of the conversion of 1-hexane is possible in the absence of catalyst for conversions up to 40% and that the results were comparables to those obtained with TIPB.

From a modeling point of view, TIPB has the advantage that its reaction mechanism is well known and its widely used in FCC research [27, 49, 50]. Figure **2-3** shows a schematic description of the catalytic cracking of TIPB. A three-step process represents this reaction [27]: (1) Dealkylation of TIPB to form 1,3-di-isopropylbenzene (DIPB) and propylene; (2) dealkylation of DIPB to form cumene and propylene: (3) dealkylation of cumene to form benzene. In each step, secondary reactions form coke.

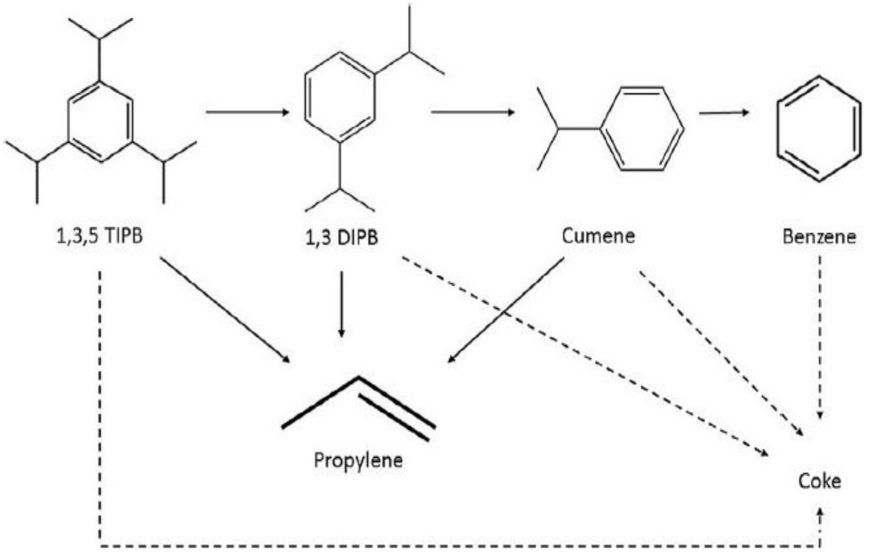

Figure 2-3: Reaction scheme that represents the catalytic cracking of TIPB [27].

The simulations in this research use the kinetic constants for the catalytic cracking of TIPB with Y-zeolite proposed by Tukur & Al-Khattaf [50]. In their research, Tukur & Al-Khattaf [50] proposed two models for catalyst deactivation, one based on time on stream (TOS) and the other based on reactant converted (RC). As these authors conclude that both models have similar performance, we selected for the simulations the model based on RC. The kinetic values used were a pre-exponential factor ($k_{0@673\ K}$) of $1.51 \times 10^{-3}\ m^3/kg_{cat} \cdot K$ and an activation energy (E_a) of $4.77 \times 10^7\ J/mol$.

To validate the correct understanding of the kinetic parameters, a batch reactor was simulated to reproduce the data obtained Tukur & Al-Khattaf [50]. It is important to note that the kinetic parameters proposed in Ref. [50] only allows for the prediction of global conversion; i.e. one cannot predict the product distribution. Figure **2-4** compares the experimental results of Tukur & Al-Khattaf [50] with those by the batch model. While minor differences are evident, the agreement between experiment and model is acceptable at the three different temperatures.

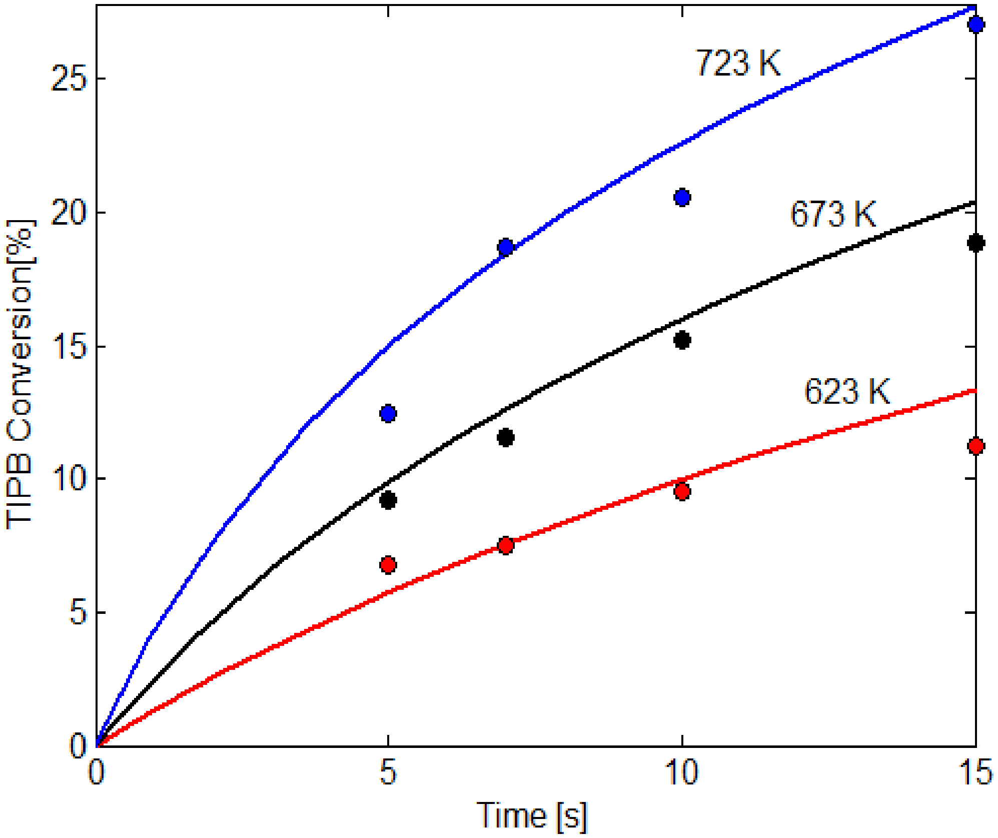

Figure 2-4: Validation of the reaction mechanism used in the simulation. Comparison of model predictions with kinetic data. Symbols: experimental data. Lines: model predictions.

2.3.2 CFD simulation

The one-dimensional simulations are particularly suitable for estimating the conversion along the reactor and the heat transfer in the first stages where the catalyst and feed mix. However, more complex models are desirable if a complete understanding of the hydrodynamics is required. Computational Fluid Dynamics (CFD) simulations can give more details of the mixing process between catalyst and feed.

Mathematical model

The CFD simulation of the downer reactor considered the three spatial dimensions and was developed using the Euler-Lagrange approach where the fluid (gas) is treated as a continuous phase while the dispersed phase (catalyst) is solved by tracking a large number of particles. The commercial CFD software Fluent V15.0 was used to discretize and solve the Navier Stokes equations of continuity, momentum, species transport, mass, and energy transfer.

The equations considered in the simulations have been widely studied and can be consulted in several references [51, 52, 53] as well as in the Ansys Fluent theory guide [54].

Mesh and boundary conditions (BC)

As is presented in detail below, the simulation domain was divided into two zones. The first domain considered the particle-heating zone, where the particles were heated from ambient temperature to a nominal temperature of around 873 K. A second zone included the entrance of the feed stream (TIPB) to the reactor zone. The particle heating zone is a 0.7 m-length, 0.013 m-diameter cylinder. The 3-D simulation has a longer heating zone than the 1-D simulation as the first one considers the exact dimensions of the reactor that includes spaces between heaters, as described in more detail below. The values of the properties and dimensions are the same in the 1-D and 3-D simulations except for T_w that, as stated above, considers the exact layout of the heaters ($T_w(0.0\ m \rightarrow 0.165\ m) = 300\ K$, $T_w(0.165\ m \rightarrow 0.615\ m) = 873\ K$, and $T_w(0.615\ m \rightarrow 0.70\ m) = 653\ K$).

A tetrahedral mesh was used for both zones. The particle-heating zone had about 600 000 elements with a mean aspect ratio of 0.88. The nitrogen and particle inlet was represented as a Mass flow inlet boundary condition. For the three different wall thermal conditions mentioned above, a no-slip shear condition was considered. A pressure outlet BC represented the exit of the particle heating zone.

The reaction zone considered 1 800 000 tetrahedral elements with a mean aspect ratio of 0.76. More elements are required to model the reaction zone than the heating zone as the first one is longer and the input of TIPB demands cells of smaller size. Figure **2-5** shows the top of the reaction zone where the refinement has been made, it also presents the BCs used. As was the case for the particle heating zone, the inlet of the nitrogen and particles coming from the heating zone was represented as a Mass flow inlet BC entering at the exit temperature obtained in the simulation of the heating zone. TIPB entered through two holes (3 mm I.D.) at a 45° angle with the vertical direction and at 573 K. The TIPB input was represented by a mass flow inlet BC. For the reactor, a Wall BC with a no-slip shear condition and a constant temperature of 823 K was considered. A Pressure outlet BC represented the exit flow of the reactor. The simulation did not consider heat transfer through radiation in the reaction zone.

The CFD simulation was simplified by neglecting the interaction between the continuous (gas) and discrete (particle) phases. In this way, the solution of the dispersed phase considers the momentum and energy contribution from the continuous phase but not vice versa. To represent the reaction, the simulation considers a pseudo-homogeneous reaction in the continuous phase and inert catalyst particles.

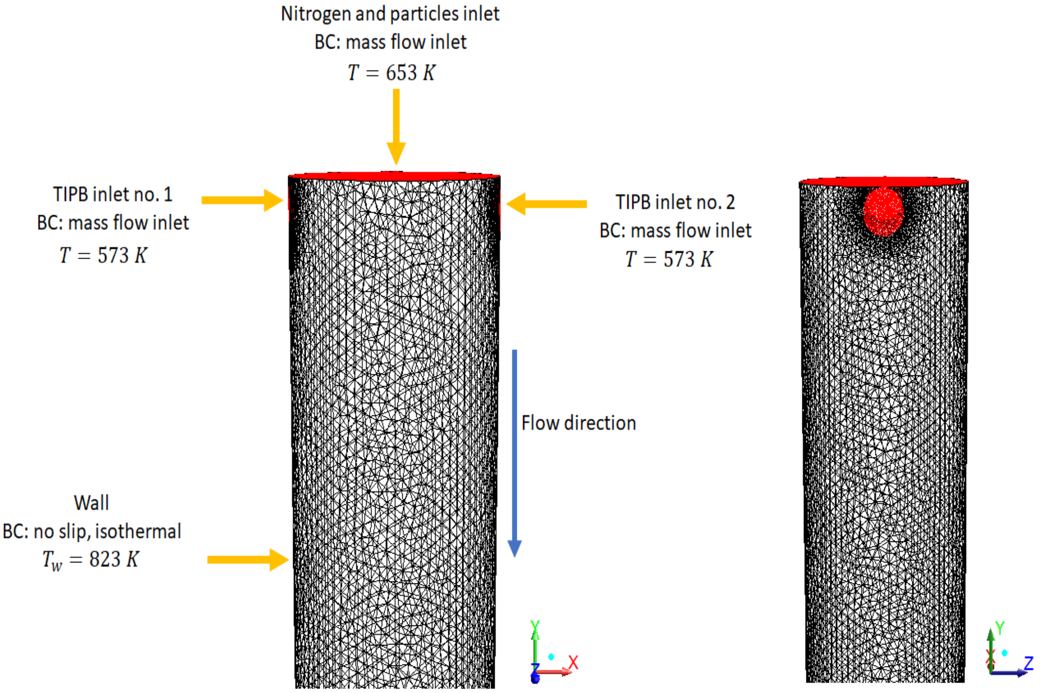
Nitrogen and particles inlet
BC: mass flow inlet
T = 653 K
TIPB inlet no. 1
BC: mass flow inlet
T = 573 K
TIPB inlet no. 2
BC: mass flow inlet
T = 573 K
Flow direction
Wall
BC: no slip, isothermal
Tw = 823 K
Y
X
Z
Y
Z

Figure 2-5: Lateral views of the mesh for the top of the reaction zone.

Physical properties and simulation parameters

The CFD simulation demanded knowledge of properties related to the heat transfer in the gas phase as well as to the solution of the momentum equation, that were not required in the 1-D model. For nitrogen the thermal conductivity (k_{N_2}), specific heat ($C_{p_{N_2}}$) and dynamic viscosity (μ_{N_2}) were calculated using a polynomial approximation that was function of the gas temperature ($f(T_g) = A_1 + A_2 \cdot T_g + A_3 \cdot {T_g}^2 + A_4 \cdot {T_g}^3 + A_5 \cdot {T_g}^4$). Table **2-1** summarizes the polynomial coefficients. The ideal gas law was used to calculate density.

Table 2-1: Coefficients to compute the nitrogen physical properties [54].

Property	A_1	A_2	A_3	A_4	A_5
k_{N_2} $(\frac{J}{s \cdot m \cdot K})$	0.00473	7.27×10^{-5}	-1.12×10^{-8}	1.45×10^{-12}	-7.87×10^{-17}
$C_{p_{N_2}}$ $(\frac{J}{kg \cdot K})$	979	0.417	-0.00117	1.67×10^{-6}	-7.25×10^{-10}
μ_{N_2} $(\frac{kg}{m \cdot s})$	7.47×10^{-6}	4.08×10^{-8}	-8.24×10^{-12}	1.31×10^{-15}	-8.17×10^{-20}

For TIPB, constant properties at 823 K were used: $k_{TIPB} = 0.05\ J/s \cdot m \cdot K$, $C_{p_{TIPB}} = 3000\ J/kg \cdot K$, and $\mu_{TIPB} = 1.4 \times 10^{-5}\ kg/m \cdot s$ [55]. It is important to note that in the particle heating zone, only the nitrogen properties are used but in the reaction zone all properties were calculated by a mass weighted mixing law. Catalyst properties have been previously mentioned in 1D-model section. Morsi-Alexander drag model for spherical particle has been considered, in the same way as in the one dimensional simulation. The models relevant for the CFD simulation are listed in Table **2-2** [56].

Table 2-2: Models used in the CFD simulation.

Models	**Method**
Multiphase	Euler - Lagrange
Solver	Pressure-based steady
Turbulence	$\kappa - \epsilon$ *model*
Discrete phase model	Activated, Inert particle
Pressure velocity coupling scheme	Phase-coupled SIMPLE
Residual convergence criteria	1.0×10^{-3}, energy 1.0×10^{-6}
Discretization Scheme	First-order upwind
Gas density	Ideal gas
Species	Species transport, volumetric reaction (only in reaction zone)
Drag model	Morsi-Alexander

2.4 Experimental section

Figure **2-6** presents a schematic representation of the experimental setup that includes four zones: 1) Evaporation, 2) Particle heating, 3) Reaction, and 4) Separation. In the Evaporation zone (N° 1 in Figure **2-6**), a precision syringe pump (New Era Pump Systems NE-8000 model) with a 200 *ml* stainless-steel syringe (partially filled to about 140 *ml*) controlled the rate of injection of the feed through an resistance-heated, steel cylinder (0.12 *m* length and 0.025 *m* diameter) packed with Ottawa sand with particle diameter between $0.85\ mm - 1\ mm$. The vaporization system reaches steady state operation approximately 25 minutes after injection begins (see Figure **2-15**, Appendix A). Nitrogen was flown (0.42 *slpm*) through the system initially to purge the evaporator and, later, to help entrain the evaporated feed. Two stainless-steel hypodermic tubes transported the N_2/feed stream into the reactor. The reactor was a clear fused quartz tube (0.013 *m* ID x 0.016 *m* OD x 1.80 *m* long) with two ports located at 45° for feed entrance located 0.70 *m* from the catalyst inlet.

The catalyst flow was controlled by a volumetric screw feeder (Schenck Process AccuRate 106M) that was calibrated for a catalyst mass flow between 0.000125 and 0.001765 kg/s (see Figure **2-16**, Appendix A). Equilibrated catalyst particles between $53 - 106$ μm were used in the experiments. A tube furnace (H1 in Figure **2-6**) of 0.45 m length, located in the particle heating zone (Zone 2 in Figure **2-6**) before the inlet of the feed ports, heated the catalyst particles up to 873 K. Nitrogen entered the quartz tube (0.13 $slpm$) and the upper part of the feeder hopper (0.035 $slpm$) to neutralize the buoyancy effect of the hot gases in the reactor and to purge the catalyst from oxygen, respectively.

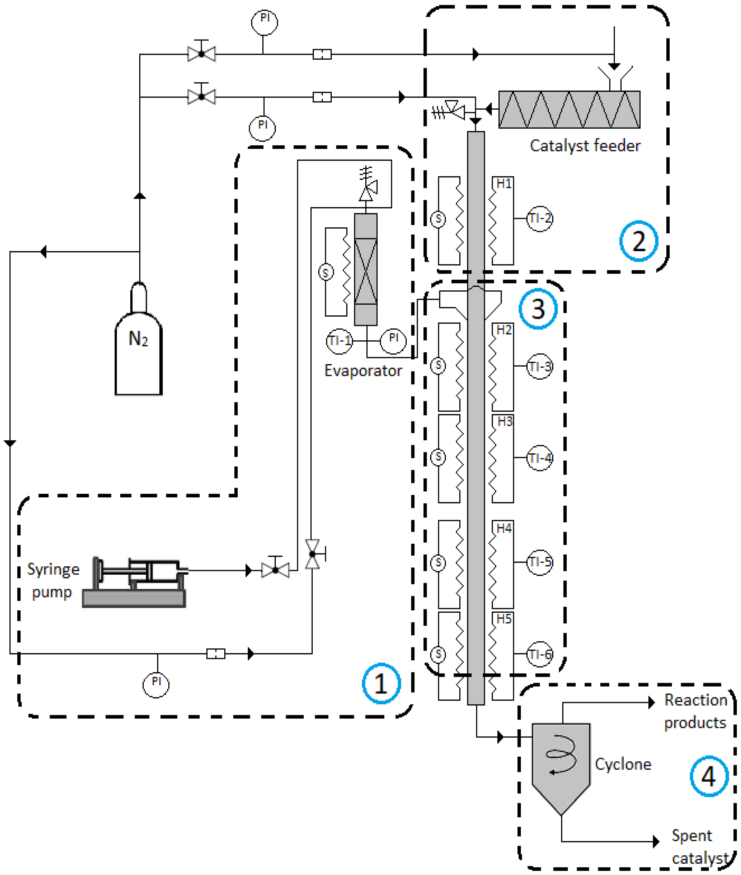
PI
PI
Catalyst feeder
H1
S
TI-2
2
3
S
Evaporator
TI-1
PI
N2
H2
TI-3
H3
TI-4
H4
TI-5
H5
TI-6
Syringe pump
PI
1
Reaction products
Cyclone
4
Spent catalyst

Figure 2-6: Experimental apparatus 1) Evaporation zone, 2) Particle heating zone, 3) Reaction zone, 4) Separation zone.

Cracking reactions take place throughout the lower part of the fused quartz tubing, i.e from the feed entrance where the evaporated feed, the catalyst, and nitrogen mix to the fused quartz end, approximately 1.10 m below. This is the reaction zone in, N° 3 in Figure **2-6**. Four additional tube furnaces with different lengths ($0.30, 0.25, 0.20$ and 0.20 m) that can be moved in the vertical position to allow optical access keep the Reaction zone at a maximum reaction temperature of 823 K. At the end of the Reaction zone, a separation cyclone removes spent catalyst from the gas reaction products, a flexible stainless steel hose is connected from the cyclone's gas outlet to an exhaust hood and the catalyst is received in a collection box with 4.5 L capacity (N° 4 in Figure **2-6**). A data acquisition system continuously logged the temperature at the outlet of the Reactant evaporation zone (TI-1 in Figure **2-6**), the temperature of the five furnaces (TI-2 to TI-6 in Figure **2-6**) and the relevant data for the optical measurements as described below. Figure **2-17** in Appendix A) presents a detail description of the reactor.

2.4.1 Optical setup

As previously mentioned, Lopez-Zamora et al. [7] demonstrated the use of a helium-neon (HeNe) laser operating in the MIR spectroscopy for monitoring the FCC reaction process. In the present study, the same optical setup proposed by Lopez-Zamora et al. was adapted to operate in the reactor in Figure **2-6** to evaluate the effect of particle flow. Figure **2-7** presents a picture of the optical setup when operating in the quartz reactor.

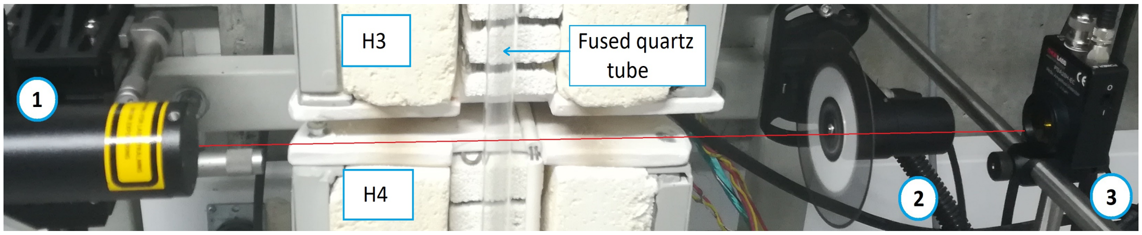

Figure 2-7: Photo of the optical setup adapted to the reactor. 1) He-Ne Laser, 2) Optical chopper and 3) Photodetector.

The optical setup includes a continuously operating Helium-Neon (HeNe) laser (Research Electro Optics, Inc.), 2949.9 cm^{-1} wavenumber (3.39 μm wavelength) working at 2800 VDC power with a beam diameter of 2.02 mm and a maximum output power of 7 mW, an optical chopper that can reach a frequency up to 1000 Hz, and a PDA20H(-EC) PbS photodetector (Thorlabs) with detection wavelength range between 1.5 μm to 4.8 μm and a Noise-equivalent power (NEP) of 1.5×10^{-10} $W/\sqrt{Hz}$. There is a separation of 0.45 m between the He-Ne laser and the photodetector.

The changes in concentration of the feed stream along the reactor were related to changes in the intensity of the laser beam according to the Beer-Lambert's law (2-19) [57].

$$-\ln \frac{I_\lambda}{I_\lambda^0} = \sigma_{\lambda,i}(T,P) \cdot n_i \cdot L = \alpha_i \tag{2-19}$$

where, I_λ^0 and I_λ are, respectively, the intensity of the radiation before and after the interaction of the laser beam with the media; $\sigma_{\lambda,i}$ is the absorption cross-section of species i

that depends on the temperature and pressure; n_i is the concentration of species i; and L is the path length. α_i (I_λ/I_λ^0) is known as absorbance and, as Equation (2-19) states, for a constant temperature, pressure, and path length the absorbance should be proportional to the concentration of species i. The last statement has one caveat and is that assumes that, for the catalytic cracking of one species, as is the case in this research, any interference of the products at the specific wavelength of the experiments is negligible. The results of Lopez-Zamora et al. [7] suggest that this is the case.

During the experiments, a significant power drift in the HeNe laser was observed (see Figure **2-18**, Appendix B). This drift was not documented in Ref. [7]; however, this behavior was previously reported by Klingbeil [58] who implemented a beam splitter and a reference detector to correct for the effect of the laser power drift. While the setup by Klingbeil [58] clearly mitigates any problem with the laser beam, because of time and budget constraints, for the present dissertation, the use of a second photodetector was not possible. Correction of the laser drift was, nevertheless, accomplished by a careful averaging and iteration procedure where feed injection was interrupted in a periodic fashion so that the variation in I_λ^0 during the experiment could be documented. Appendix B explains in detail this correction procedure.

2.5 Results

The results are discussed in two sections. The first section compares the results from the 1D and the CFD simulation with experimental data. This comparison gives inside into the phenomena taking place in the reactor. A second section presents the results of the optical measurements.

2.5.1 Simulation

Figure **2-8** shows the variation of gas and particle temperature along the heating zone as predicted by the 1D and the CFD simulations and as measured in the experiments. Both experiments and simulations considered a flow of N2, feed, and particles as described in Section 2.3. It is important to point out that the CFD simulation considered a zone without heater from 0 m to 0.15 m in the reactor and from 0.62 m to 0.70 m. The 1D simulation was only carried for the 0.45 m where the heater acted on the fuzed-quartz reactor.

The experimental data show that the gas temperature is already 820 K, at 0.38 m from the gas entrance. While this temperature is for the gas, as the thermocouple was sensing the gas phase, this value should give a good indication of the actual particle temperature as the difference between both phases is very low, as both models indicate. The temperature sensed by the thermocouple varied between 820 K and 880 K in the heating zone.

The maxima of 880 K in the center of the heating zone could be associated with the fact that particles are heating -for distances below 0.4 m- and cooling -for distances above 0.55 m-.

Although only three experimental measurements are available in the region where the heater operates, the results suggest that the 1D model captures the trend of temperature. The results of the CFD model predict a faster particle heating process that renders a gas and particle temperature of 875 K almost immediately after entering the reactor. This prediction of relatively fast heating by the CFD is probably incorrect and it is the result of the fact that the CFD simulation did not consider heat transfer from the particle to the gas phase. Therefore, the gas phase did not register thermal inertia associated with heating the particle flow.

Convective heat transfer contributes about 95% of total heat transfer, it has been widely studied that radiative heat transfer becomes relevant at temperatures higher than 973 K [59].

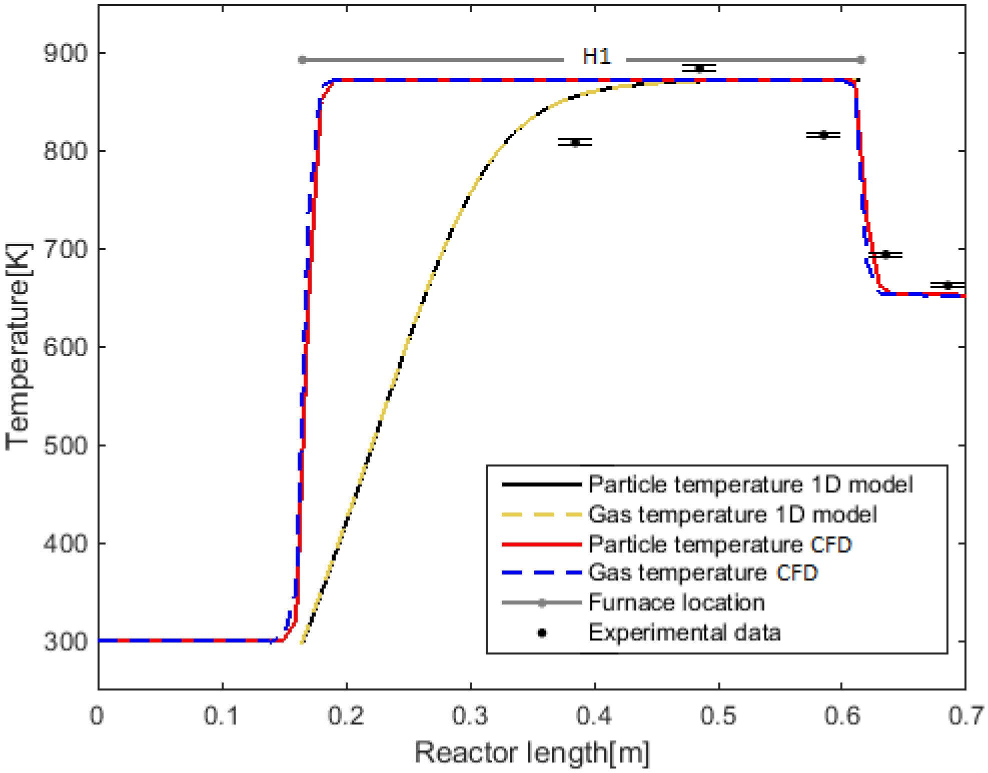

Figure 2-8: Temperature profile along the heating zone. Results are for simulations results of the 1D and CFD simulations and from the experiments. Error bars represent one standard deviation.

Figure **2-9** presents the velocity profile as predicted by the 1D and the CFD simulation. Contrary to Figure **2-8** that only presented results for the Heating zone, Figure **2-9** presents the complete reactor domain, from the Heating zone to the Reaction zone. As was the case in Figure **2-8** , the 1D simulation only considered particular regions, this is where the heater is present in the Heating zone and after the entrance of the feed in the Reactor zone. The CFD simulation considered the complete domain.

Figure **2-9** makes evident the differences between the Heating zone and the Reaction zone as the entrance of the Feed in the later significantly enhances the gas velocity. The other changes in gas velocity along the reactor can be traced to changes in gas temperature, as is discussed below. The slight difference between the 1D and CFD simulations after the feed entrance stem from the fact that the CFD simulation considers the loss of momentum after the entrance of the feed (see Figures **2-20** and **2-21**, Appendix C) and, as explained below, because the predicted conversion is lower for the CFD case. Lower conversion implies a higher gas density and, therefore, a lower gas velocity.

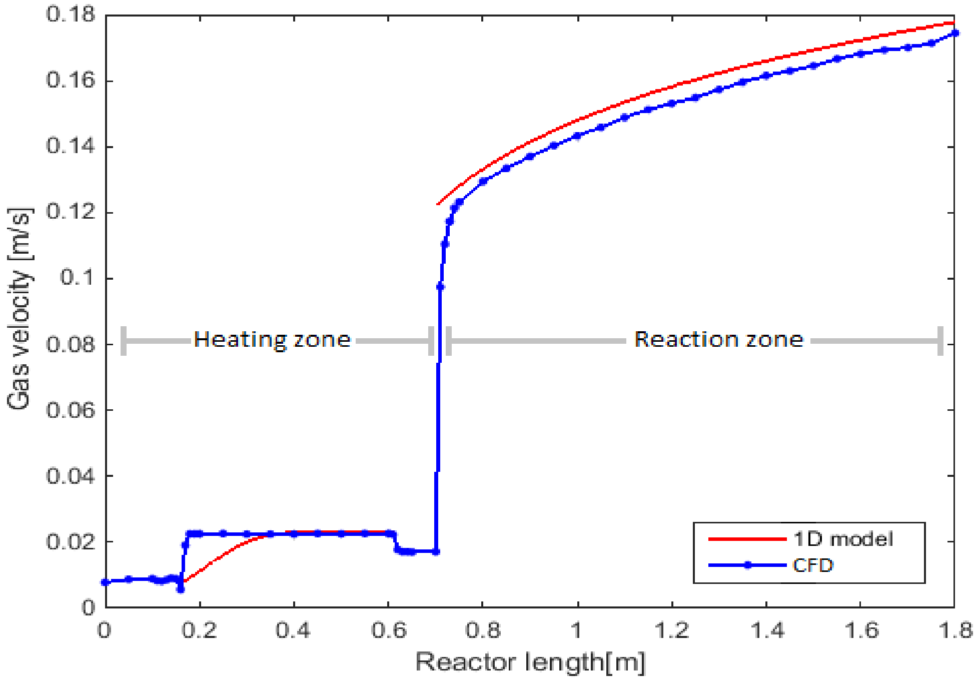

Figure 2-9: Gas velocity profile along the reactor as predicted by the 1D and the CFD simulations.

The predictions of particle velocity in Figure **2-10** present more differences between the two simulations than those found for the gas velocity comparison. For the CFD simulation, only the velocity component in the axial direction (Y) (see Figure **2-5**) was considered in this figure. Both simulations predict that the particle velocity decreases in the first stages in the reactor as it loses momentum to the gas phase. Note that the particle velocity is one order of magnitude higher than that of the gas. Differences in the prediction of setting velocity in the Heating zone between both models are probably related to differences in the drag coefficient (Eq. (2-4)) as the CFD simulations have a more complete description of the gas and temperature field that affect the calculation of the particle velocity.

At 0.70 m, particles accelerate because of the augmented gas flow as the feed the reactor that is captured by both models. However, once in the Reactor zone the CFD simulation predicts a significant decrease in particle velocity associated by a loss of momentum because of the entrance of the feed that the 1D simulation does not capture. This and the lower gas velocity in Figure **2-9** explain the lower particle velocity predicted by the CFD simulation in Figure **2-10**.

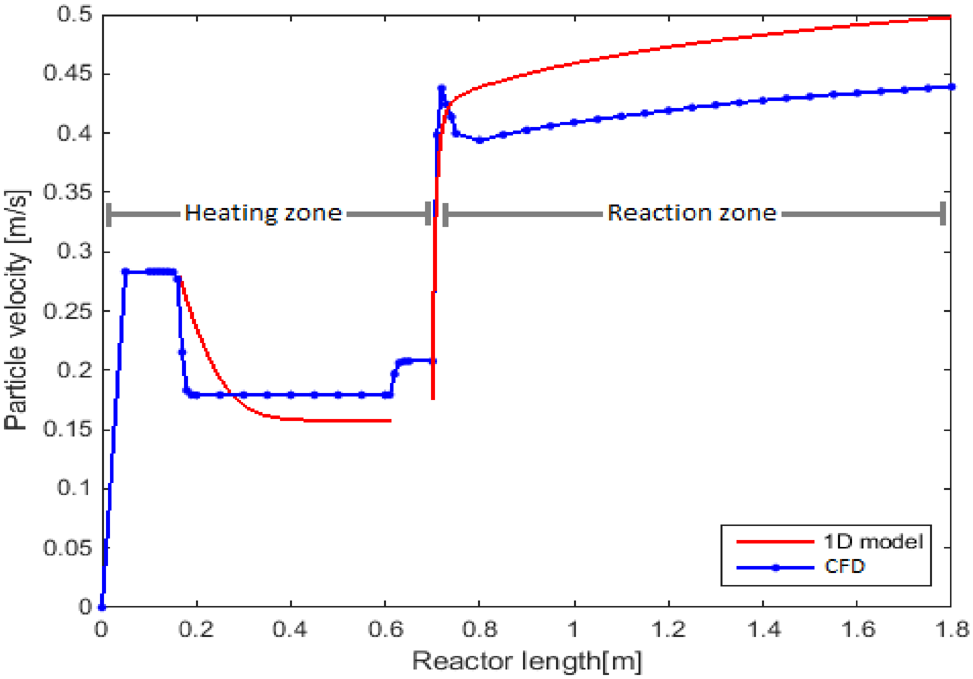

Figure 2-10: Particle velocity profile along the reactor as predicted by 1D and CFD simulations.

The predicted conversion is 17% and 19% for the CFD and 1D simulation, respectively, as Figure **2-11** shows. The CFD simulation captures hydrodynamic effects that negatively affect the reaction yield and which can not be appreciated in the 1D simulation. The entrance of the feed, as well as the flow in the tube, causes radial dispersion, backmixing, swirl, and non-homogeneous temperature profiles (see Figures **2-20** and **2-21**, Appendix C). In any case, the results by both simulations are within the conversion range reported by Tukur & Al-Khattaf [50].

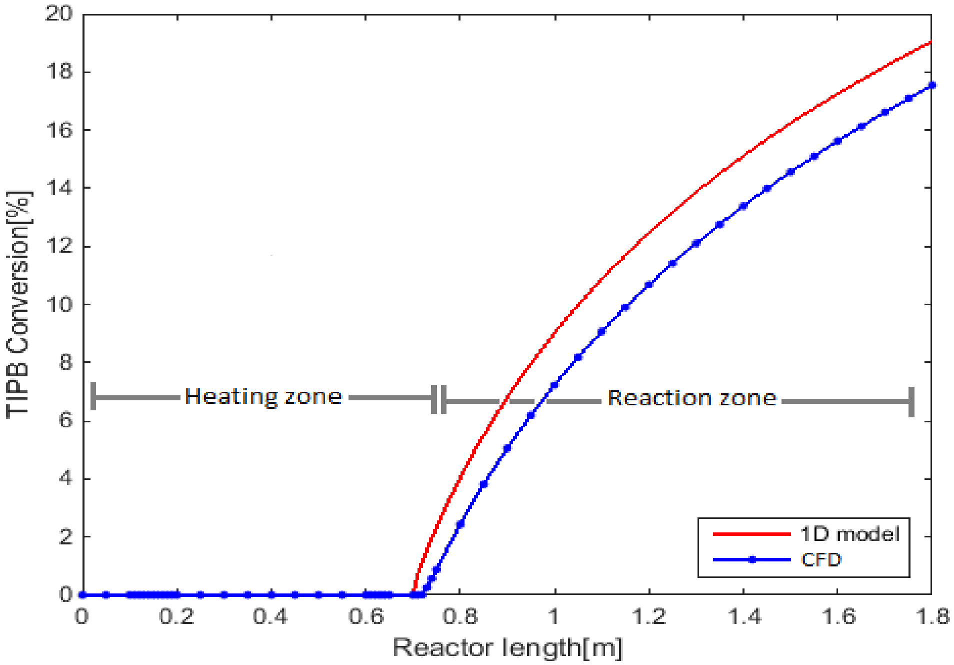

Figure 2-11: Predicted global conversion by the 1D and CFD simulations.

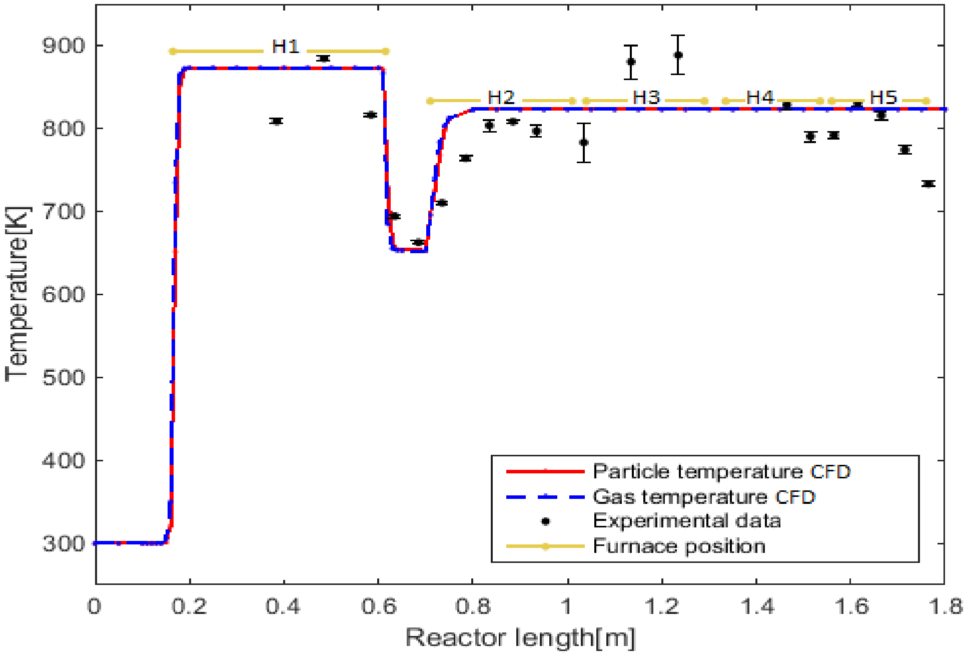

Figure 2-12: Comparison of the temperature profile along the reactor as predicted by the CFD model and as measured in the experiments. Error bars represent one standard deviation.

A final plot, Figure **2-12**, compares the gas temperature profile measured along the reactor with the CFD predictions. Although CFD only considered a one-way interaction (from the gas to the particle) agreement is acceptable. There are three regions, however, were agreement is just acceptable: (i) at 0.4 m where, as explained above, the CFD model tends to overpredict the rate at which particles heat; (ii) between 1.1 m and 1.3 m where measurements with a long thermocouple became difficult; and (3) at the Reaction zone exit where the furnace losses energy to the uninsulated reactor end but this effect is not captured in the simulation.

The simulations in figures **2-8** to **2-12** served two purposes. First, they helped in the design of the system in Figure **2-6**. Secondly, they were fundamental in the understanding of the momentum, energy, and mass transfer phenomena in the reactor. This understanding helped to have success in the optical measurements described below.

2.5.2 Optical measurements

The initial experiments were with 1-hexene (C_6H_{12}, 84.16 g/mol, boiling point = 336 K). Figure **2-13** presents the variation of the fractional transmission with the molar fraction of 1-hexene with and without particles and at different temperatures. As the molar fraction of 1-hexene increases, I/I_0 decreases as the amount of light absorbed is higher. Interestingly, when the molar fraction is only 0.45, I/I_0 is already almost 0 which indicates the high sensitivity of the optical system to the concentration of 1-hexene.

An observation of the variation of I/I_0 with the molar fraction of 1-hexene demonstrates that when the molar fraction of 1-hexene is higher than 0.2 the system does not obey the Beer-Lambert's law, i.e. I/I_0 does not linearly vary with the concentration of 1-hexene. Beer-Lambert's law nonlinearity for concentrations higher than 10 mM have been previously reported [60].

When at the same temperature (373 K), but in the presence of equilibrated catalyst, the variation of I/I_0 with the molar fraction of 1-hexene was evaluated, a linear trend was obtained. Furthermore, the value of I/I_0, for the same molar fraction of 1-hexene, increased. This result was somehow unexpected as light scattering should decrease the value of I_0 in a magnitude similar to the reduction in I as both reductions depend on the number of particles flowing in the system. One possible explanation for the significant increase in I/I_0 in the presence of the catalyst is the absorption of 1-hexene in the catalyst as is discussed in Appendix C. Nevertheless, the results at 373 K in the presence and absence of catalyst are encouraging as they indicate that the measurement of 1-hexene in the reactor in the presence of a catalyst is possible and that the Beer-Lambert's law can be used to estimate the 1-hexene concentration in the range of molar fractions in Figure **2-13**.

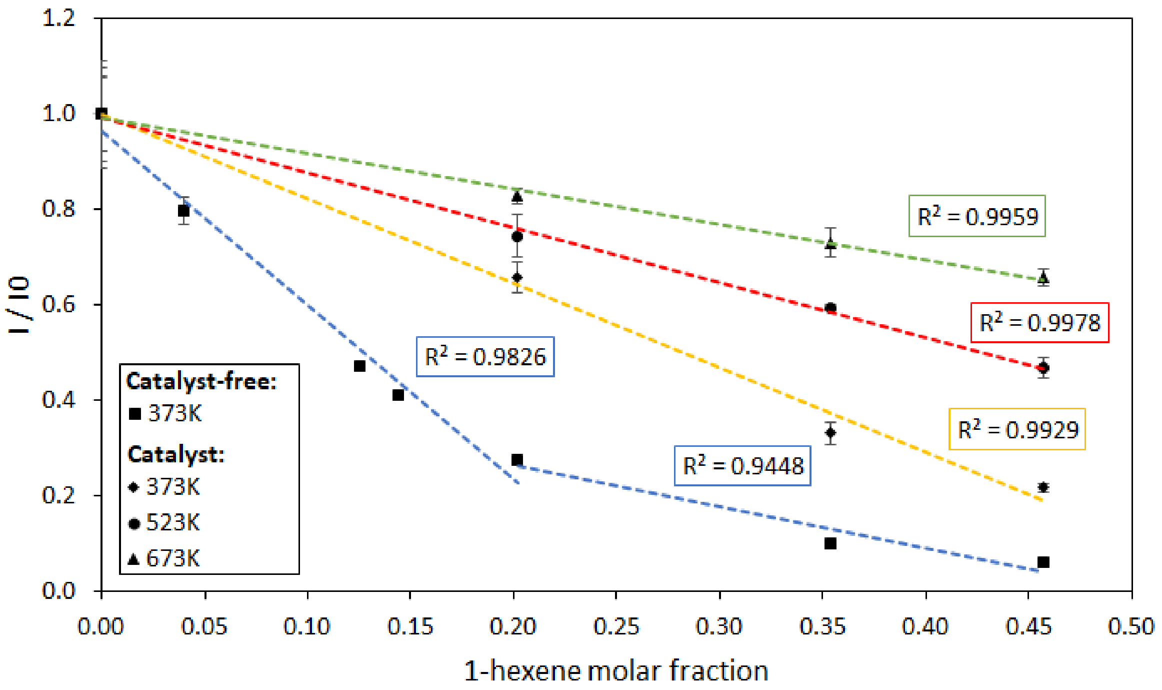

Figure 2-13: Variation of the fractional transmission (I/I_0) with the molar fraction of 1-hexene at different temperatures and in the presence and absence of catalyst.

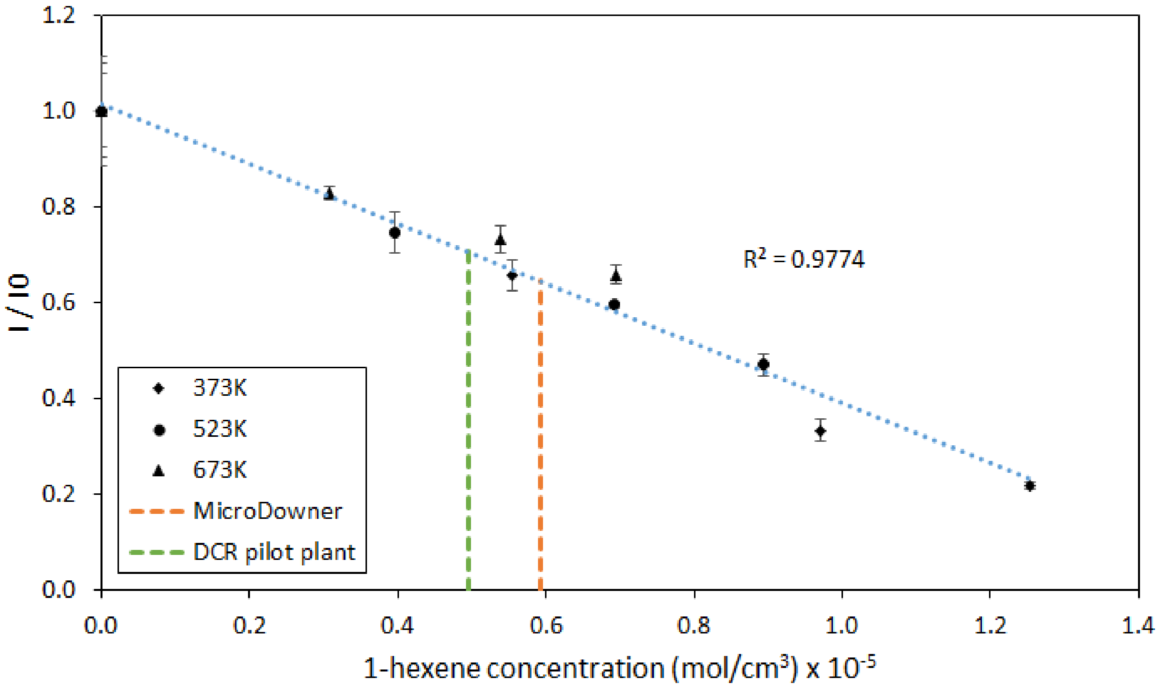

Figure 2-14: Fractional transmission at different 1-hexene concentrations.

For the experiments at higher temperatures in Figure **2-13**, it is evident that for a given value of 1-hexene the fractional transmission increases as the molar concentration decreases. This is expected as the higher the temperature, the lower the molar concentration of 1-hexene. Figure **2-14** presents the same data as in Figure **2-13**, but this time in the abscissa the 1-hexene concentration is presented as molar concentration instead of molar fraction. Clearly, all the temperature lines collapse into one sole line. This result indicates that even in the presence of catalyst particles this method can track the conversion of 1-hexene in a temperature range relevant for FCC (673 K). While the absorption cross section of 1-hexene depends on temperature, in the range evaluated in this research that dependence is low, an observation that further boosters the applicability of this laser technique for the evaluation of the conversion of hydrocarbons during FCC reactions.

Figure **2-14** also presents typical concentration values for the Microdowner® unit [11] and the commercial Grace's DCR® pilot plant [61]. The concentrations in these two units lay in the range of 1-hexene concentrations in Figure **2-14**. One more result that indicates the potential application of the laser technology for FCC characterization.

2.6 Conclusions

Starting from conceptual design, a gas-solid, laboratory-scale downer reactor that allows the use of optical techniques and which can operate at conditions similar to those of industrial FCC units was built. Based on 1D and CFD simulations, a minimum length of 0.35 m has been found to preheat catalyst particle up to 873 K, because of that, a tube furnace of 0.45 m has been used for this task. The predicted conversion in the furnace varied between 17% and 19% for a 1.10 m reaction zone length operating at 823 K. A CFD simulation captures the most significant hydrodynamic effects in the mixing point that affect the global performance on the equipment and complemented the results of the 1D simulation.

Experiments using 1-hexene as a model compound for FCC were carried out to validate the performance of a laser operating in the mid-infrared at 3.39 μm wavelength when detecting different concentrations of 1-hexene in the presence of a solid catalyst. Even in the presence of the catalyst, the laser technique captures changes in reactant concentration at temperature and concentrations typical of those observed in FCC conditions.

Appendix A. Overall setup

For a set value of 823 K, the reactant evaporation zone takes up to 25 minutes to reach a constant gas temperature near 620 K at the outlet.

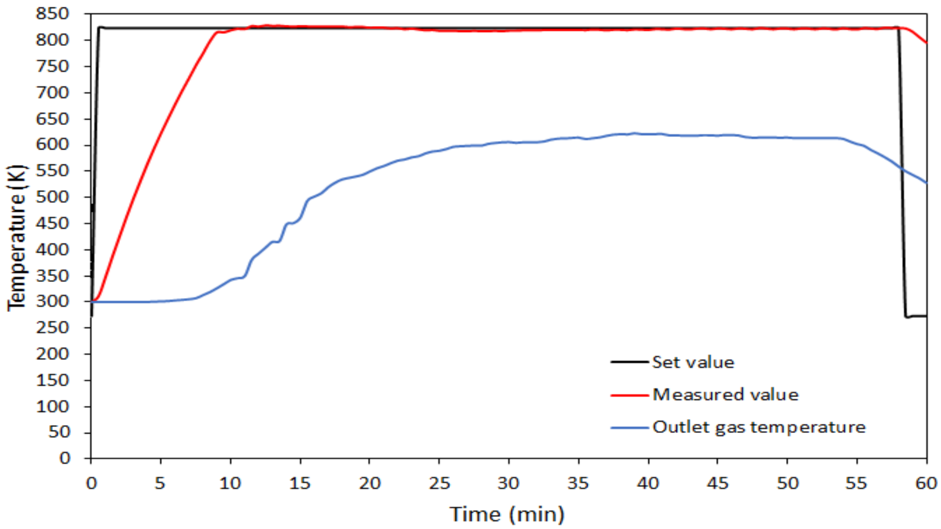

Figure 2-15: Variation of temperature with time in the Reactant evaporation zone.

Based on the result of the calibration curve for the volumetric screw feeder, 163 RPM are needed for reaching a catalyst mass flow rate of 0.0005 kg/s.

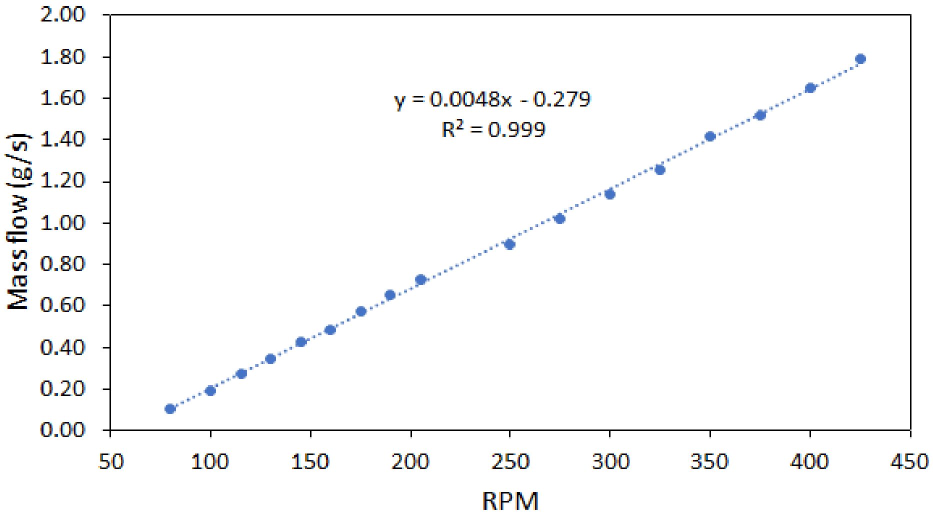

Figure 2-16: Calibration curve for the volumetric screw feeder.

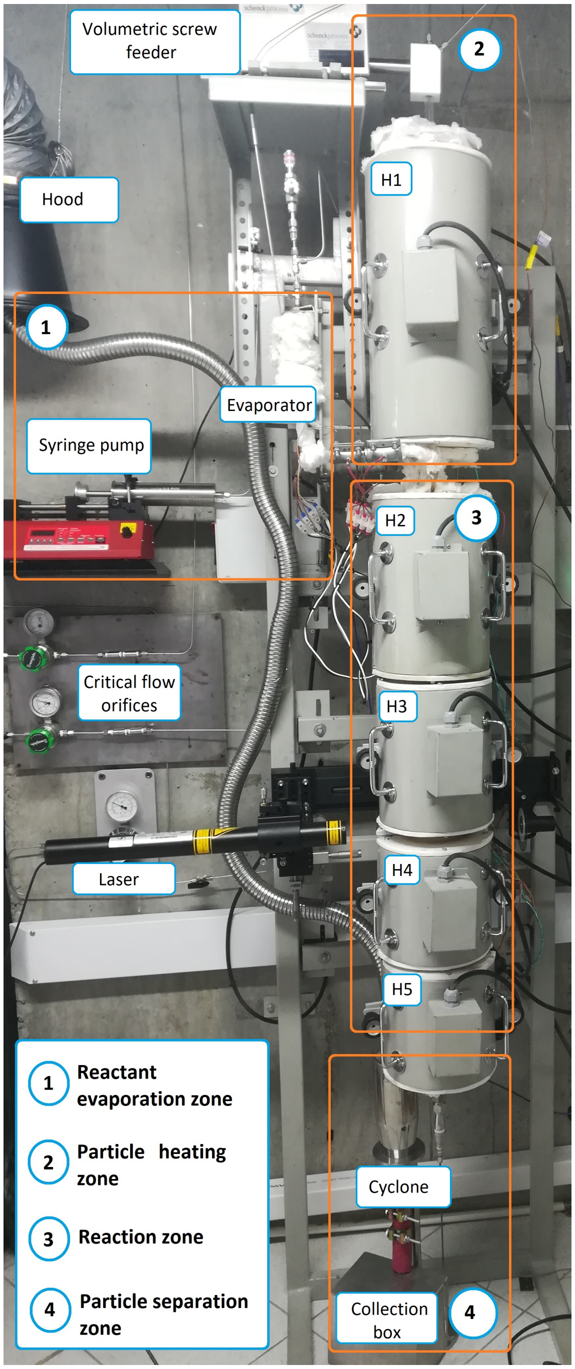
Volumetric screw feeder
2
H1
Hood
1
Evaporator
Syringe pump
H2
3
Critical flow orifices
H3
Laser
H4
H5
1 Reactant evaporation zone
2 Particle heating zone
3 Reaction zone
4 Particle separation zone
Cyclone
Collection box
4

Figure 2-17: Actual setup picture and the four zones considered.

Appendix B. Correction to the Optical Signal because of Laser Power Drift

Figure **2-18** shows the laser power drift when the distance between the laser and the photodetector was 5 cm and only the optical chopper was between them. After two hours of laser operation (7200 s) the fluctuations in laser intensity with time decreases but is still very intense, furthermore, there is not a clear pattern.

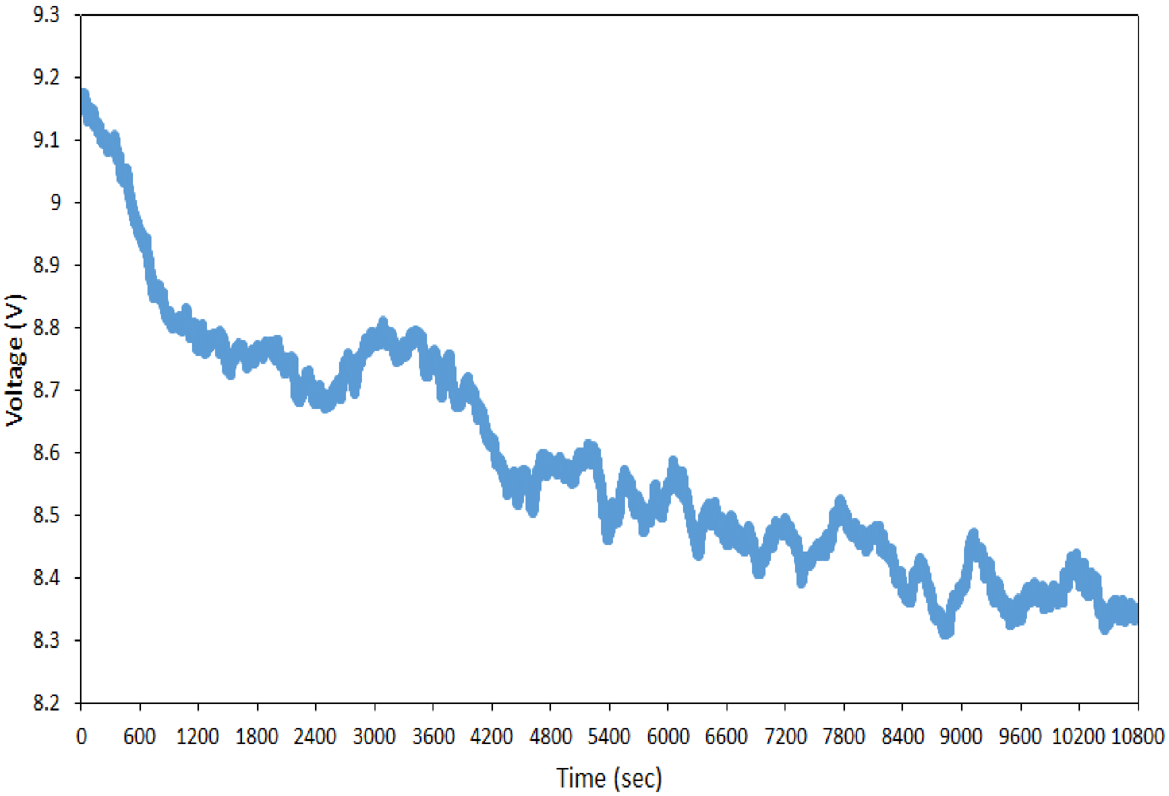

Figure 2-18: Variation in laser intensity with time. Only the chopper was between the laser and the detector.

Figure **2-19** illustrates how the experiments were conducted to correct for the laser power drift. Basically, the feed injection was alternated with periods with a flow of N_2 equivalent to the feed flow while I was recorded when the feed was flowing, I_0 was recorded in the presence of N_2.

In Figure **2-19**, the uneven numbers (1, 3, 5, 7 and 9), i.e. zones with higher voltage, indicate periods of time when only nitrogen and catalyst were flowing. In the same way, even numbers (2, 4, 6 and 8) represent periods of time when the reactant (1-hexene) was injected. While the peaks and valleys in the signal are because of the detection of particles passing through the laser signal, the average signal between each section also changes because of the laser drift. As some disruption can be expected when the flow is switched from N_2 to the feed and vice-versa, the following procedure was taken to obtain an average laser signal in each zone.

1. Find the highest value of voltage in N_2 Injection i and average data 15 seconds before and 15 seconds after that maximum, always guaranteeing that the data is collected from the period of time when only N_2 is flowing.
2. Repeat (1) for N_2 Injection $i + 2$.
3. Average the signal from (1) and (2) so that a total of 60 seconds of data have been recorded. This is the value of I_0 used to compute I/I_0 for feed Injection $i + 1$.
4. I is simply calculated as the average signal 60 s after injection of the feed has stopped.
5. I/I_0 for feed Injection $i + 1$ is calculated as the ratio of I_0 calculated in (1) through (3) and I in (4).
6. Repeat 1 through 5 for Injection $i + 3$.

Table **2-3** illustrates the procedure for the data in Figure **2-19**. For the experiment of this example, a fractional transmission (I_λ/I_λ^0) of 0.731 with a standard deviation of 0.030 was obtained. These are the values reported in Figures **2-13** and **2-14**.

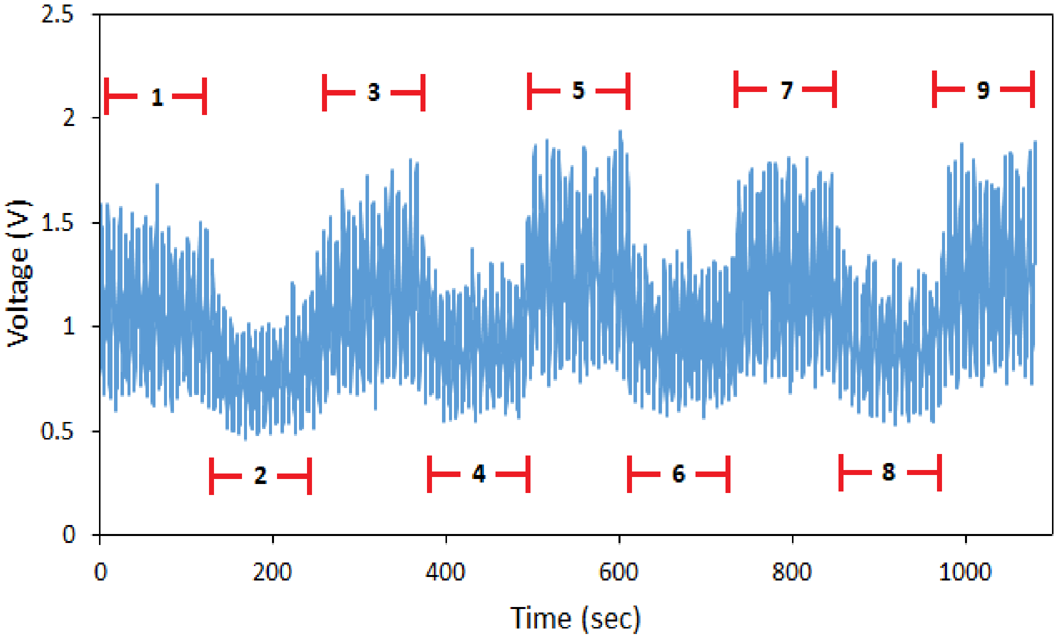

Figure 2-19: Typical behavior of voltage in time for an experiment with catalyst and 1-hexene.

Table 2-3: Data obtained from Figure **2-19**.

	I_λ^0	I_λ	I_λ/I_λ^0
	$1.144_{(1\to3)}$	$0.798_{(2)}$	0.698
	$1.236_{(3\to5)}$	$0.929_{(4)}$	0.752
	$1.261_{(5\to7)}$	$0.959_{(6)}$	0.760
	$1.266_{(7\to9)}$	$0.906_{(8)}$	0.716
Mean	1.227	0.898	0.731
SD	0.057	0.070	0.030

Appendix C. Supplementary results

This appendix presents supplementary results that, to improve readability, were not included in the main section.

Mixing point CFD result

Figures **2-20** and **2-21** show, where the feed and the flow of nitrogen and catalyst mix, the predictions of the CFD simulation as vectors colored by velocity (Figures **2-20**) and temperature (Figure **2-21**). Swirl and backmixing are evident. These effects cause a departure from plug flow in concentration and temperature that the 1D simulation does not capture.

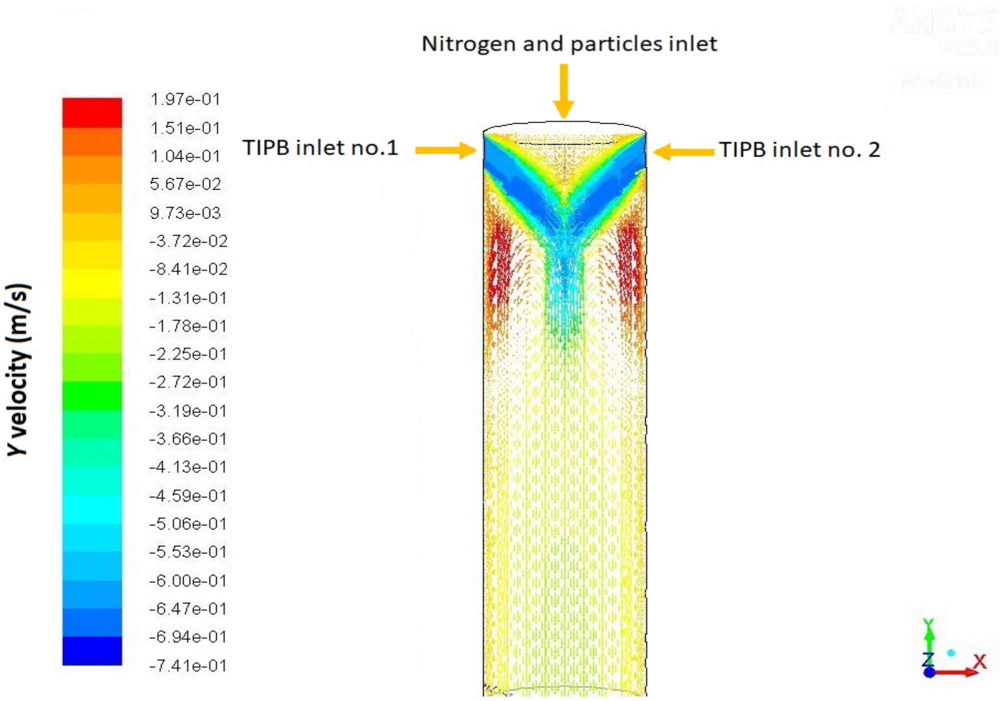

Figure 2-20: Velocity vectors colored by Y velocity in the region were the feed (entering from both sides at the top of the figure) and catalyst and nitrogen mix.

1-hexene absorption

To evaluate 1-hexene absorption on the catalyst, the feeder hopper was load with fresh catalyst at the top and catalyst that have been collected after one pass through the reactor. The experiments, conducted at room temperature, give evidence of the absorption of 1-hexene by the catalyst as the laser intensity decreases when the 1-pass catalyst is injected. Figure **2-22** indicates a lower 1-hexene concentration (higher signal) in the presence of fresh catalyst. This absorption is probably responsible for the reduction in signal observed when catalyst enters the reactor as documented in Figure **2-13**.

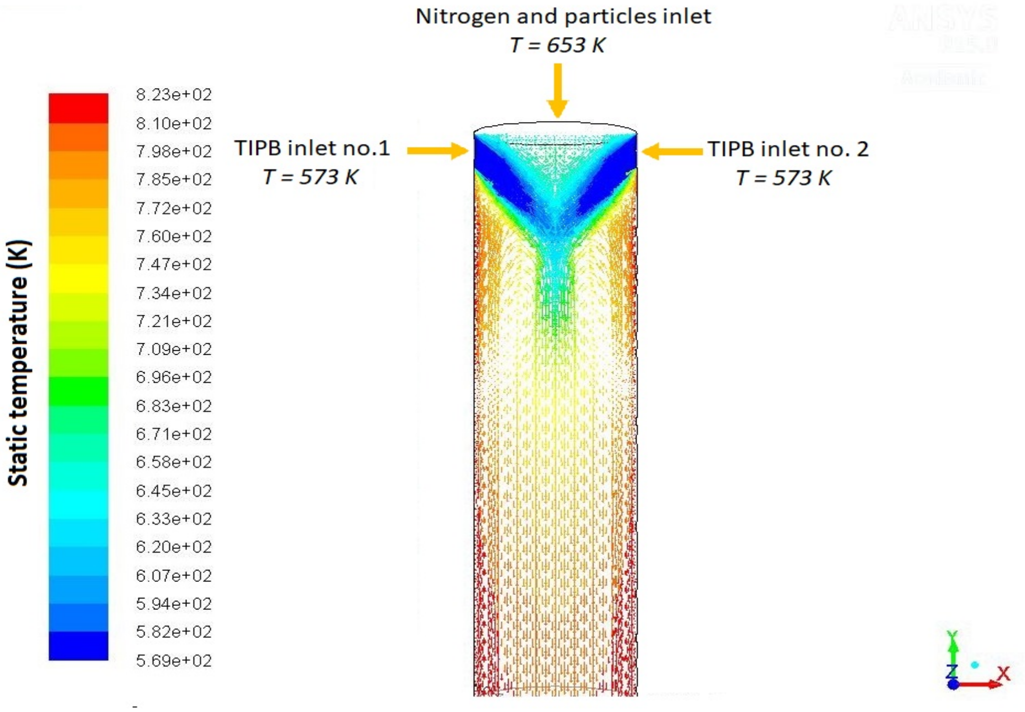
Nitrogen and particles inlet
T = 653 K
TIPB inlet no.1
T = 573 K
TIPB inlet no. 2
T = 573 K
Static temperature (K)
8.23e+02
8.10e+02
7.98e+02
7.85e+02
7.72e+02
7.60e+02
7.47e+02
7.34e+02
7.21e+02
7.09e+02
6.96e+02
6.83e+02
6.71e+02
6.58e+02
6.45e+02
6.33e+02
6.20e+02
6.07e+02
5.94e+02
5.82e+02
5.69e+02
Y
Z
X

Figure 2-21: Velocity vectors colored by temperature.

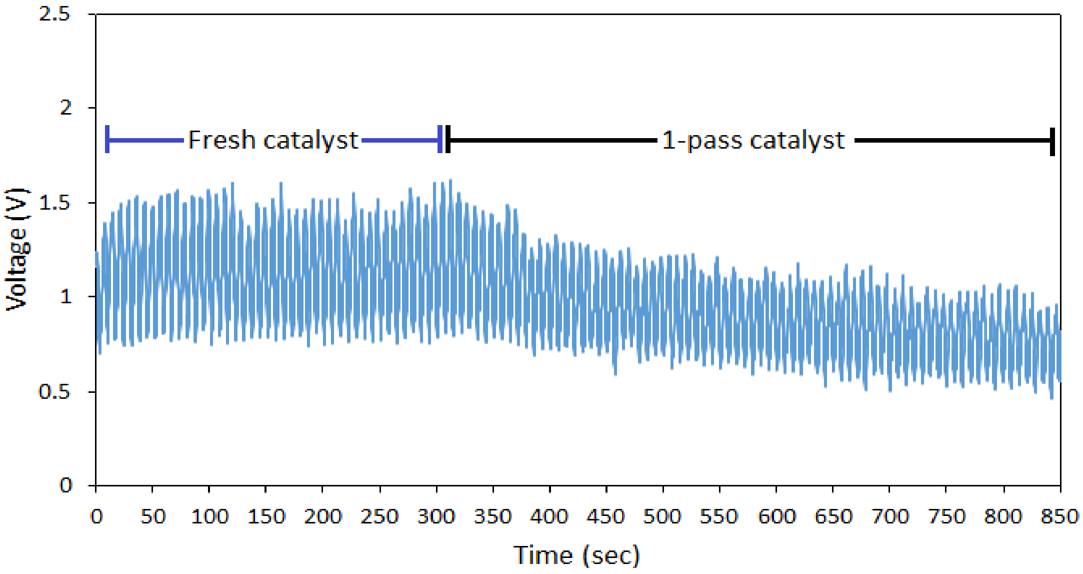

Figure 2-22: Variation of laser intensity when fresh catalyst (0 *s* - 300 *s*) and 1-pass catalyst (300 *s* - 850 *s*) enter a flow of 1-hexene at atmospheric temperature.

3 Conclusions and future work

3.1 Conclusions

An FCC laboratory-scale downer reactor that allows the use of an optical technique for monitoring reaction progress even in catalyst presence was designed and built. The design, based on a coupled 1-D (for the chemistry) and CFD (for the hydrodynamics) simulation indicated that a length of 0.45 m was required to guarantee a temperature of 823 K at the entrance of a reaction zone where TIPB was added to the system. The 1-D model predicted a conversion of TIPB of the order of 20% that could not be verified in the experiments. However, the predictions of gas temperature in the system agreed with the final measurements.

Experiments with 1-hexene as surrogate compound at FCC operating conditions demonstrate the reactor capability for in situ measurements with a He-Ne laser operating at 3.39 μm. In particular, the fractional transmission (I/I_0) had a very good linear correlation with the 1-hexene molar concentration (0.25×10^{-5} mol/cm^3 to 1.25×10^{-5} mol/cm^3) at temperatures varying from 373 K to 673 K. The fact that this range of concentration includes the concentration of laboratory-scale units used for studying FCC gives confidence on the viability of applying this laser technique in the evaluation of the FCC conversion.

3.2 Future work

CFD simulations should include four-way coupling to properly assess the effect of particles in the flow. These simulations should be conducted in future work.

To minimize the error in the optical measurement given the documented laser power drift, it is indispensable the use of a laser beam splitter and another photodetector to do a continuous follow-up of the transmitted light intensity.

The experimental technique should be further validated with more complex hydrocarbons such as TIPB. The actual measurement of the advance of the TIPB reaction should be provided.

References

[1] ETC Vogt and BM Weckhuysen. Fluid catalytic cracking: recent developments on the grand old lady of zeolite catalysis. *Chemical Society Reviews*, 44(20):7342–7370, 2015.

[2] P O'Connor. Catalytic cracking: the future of an evolving process. In *Studies in Surface Science and Catalysis*, volume 166, pages 227–251. Elsevier, 2007.

[3] E Rodríguez, A Gutiérrez, R Palos, FJ Vela, JM Arandes, and J Bilbao. Fuel production by cracking of polyolefins pyrolysis waxes under fluid catalytic cracking (fcc) operating conditions. *Waste Management*, 93:162–172, 2019.

[4] E Ivanchina, E Ivashkina, and G Nazarova. Mathematical modelling of catalytic cracking riser reactor. *Chemical Engineering Journal*, 329:262–274, 2017.

[5] P Liu, Z Zhang, M Jia, X Gao, and J Yu. Zsm-5 zeolites with different sio2/al2o3 ratios as fluid catalytic cracking catalyst additives for residue cracking. *Chinese Journal of Catalysis*, 36(6):806–812, 2015.

[6] R Sadeghbeigi. *Fluid catalytic cracking handbook: An expert guide to the practical operation, design, and optimization of FCC units*. Elsevier, Oxford, UK, 2012.

[7] S Lopez-Zamora, A Alkhlel, and H De Lasa. Monitoring the progress of catalytic cracking for model compounds in the mid-infrared (mir) 3200–2800 cm- 1 range. *Chemical Engineering Science*, 192:788–802, 2018.

[8] J Kayser. Versatile fluidized bed reactor, May 30 2000. US Patent 6,069,012.

[9] H De Lasa. Riser simulator, April 7 1992. US Patent 5,102,628.

[10] MP Helmsing, M Makkee, and JA Moulijn. Development of a bench scale fcc microriser. Technical report, American Chemical Society, Washington, DC (United States), 1995.

[11] A Corma, C Martınez, FV Melo, L Sauvanaud, and JY Carriat. A new continuous laboratory reactor for the study of catalytic cracking. *Applied Catalysis A: General*, 232(1-2):247–263, 2002.

[12] AM Squires. The story of fluid catalytic cracking: The first "circulating fluid bed". In *Circulating fluidized bed technology*, pages 1–19. Elsevier, 1986.

[13] J-X Zhu, Z-Q Yu, Y Jin, JR Grace, and A Issangya. Cocurrent downflow circulating fluidized bed (downer) reactors—a state of the art review. *The Canadian Journal of Chemical Engineering*, 73(5):662–677, 1995.

[14] D Li, M B Ray, AK Ray, and J Zhu. A comparative study on hydrodynamics of circulating fluidized bed riser and downer. *Powder technology*, 247:235–259, 2013.

[15] H Zhang, J-X Zhu, and M Bergougnou. Flow development in a gas-solids downer fluidized bed. *The Canadian Journal of Chemical Engineering*, 77(2):194–198, 1999.

[16] EF Sousa-Aguiar. Y zeolites as a major component of fcc catalysts: Main challenges in the modification thereof. In *Zeolites and Zeolite-Like Materials*, pages 265–282. Elsevier, 2016.

[17] S Al-Khattaf. The influence of y-zeolite unit cell size on the performance of fcc catalysts during gas oil catalytic cracking. *Applied Catalysis A: General*, 231(1-2):293–306, 2002.

[18] SM Sadrameli. Thermal/catalytic cracking of hydrocarbons for the production of olefins: A state-of-the-art review i: Thermal cracking review. *Fuel*, 140:102–115, 2015.

[19] P Venuto and ET Habib. *Fluid catalytic cracking with zeolite catalysts.* Marcel Dekker, Inc., New York, USA, 1979.

[20] M Guisnet and P Magnoux. Organic chemistry of coke formation. *Applied Catalysis A: General*, 212(1-2):83–96, 2001.

[21] A Corma and L Sauvanaud. Fcc testing at bench scale: New units, new processes, new feeds. *Catalysis today*, 218:107–114, 2013.

[22] ASTM D3907/D3907M. *Standard Test Method for Testing Fluid Catalytic Cracking (FCC) Catalysts by Microactivity Test.* American Society for Testing and Materials International, West Conshohocken, USA, 2019.

[23] P O'Connor and MB Hartkamp. A microscale simulation test for fcc development. *American Chemical Society, Division of Petroleum Chemistry, Preprints;(USA)*, 33(CONF-880939–), 1988.

[24] T Myrstad and H Engan. Testing of resid fcc catalysts in mat. *Applied Catalysis A: General*, 171(1):161–165, 1998.

[25] C Delattre, M Forissier, I Pitault, D Schweich, and JR Bernard. Improvement of the microactivity test for kinetic and deactivation studies involved in catalytic cracking. *Chemical engineering science*, 56(4):1337–1345, 2001.

[26] D Wallenstein, M Seese, and X Zhao. A novel selectivity test for the evaluation of fcc catalysts. *Applied Catalysis A: General*, 231(1-2):227–242, 2002.

[27] S Al-Khattaf, JA Atias, K Jarosch, and H De Lasa. Diffusion and catalytic cracking of 1, 3, 5 tri-iso-propyl-benzene in fcc catalysts. *Chemical engineering science*, 57(22-23):4909–4920, 2002.

[28] J Mazumder and H De Lasa. Fluidizable ni/la2o3-γal2o3 catalyst for steam gasification of a cellulosic biomass surrogate. *Applied Catalysis B: Environmental*, 160:67–79, 2014.

[29] MA Den Hollander, M Makkee, and JA Moulijn. Coke formation in fluid catalytic cracking studied with the microriser. *Catalysis today*, 46(1):27–35, 1998.

[30] X Dupain, ED Gamas, R Madon, CP Kelkar, M Makkee, and JA Moulijn. Aromatic gas oil cracking under realistic fcc conditions in a microriser reactor. *Fuel*, 82(13):1559–1569, 2003.

[31] MA Den Hollander, M Wissink, M Makkee, and JA Moulijn. Gasoline conversion: reactivity towards cracking with equilibrated fcc and zsm-5 catalysts. *Applied Catalysis A: General*, 223(1-2):85–102, 2002.

[32] A Lanza, M Islam, and H De Lasa. Particle cluster sizing in downer units. applicable methodology across downer scale units. *Powder technology*, 316:198–206, 2017.

[33] X Gao, C Wu, Y-W Cheng, L-J Wang, and X Li. Experimental and numerical investigation of solid behavior in a gas–solid turbulent fluidized bed. *Powder technology*, 228:1–13, 2012.

[34] GJ De Castilho and MA Cremasco. Comparison of downer and riser flows in a circulating bed by means of optical fiber probe signals measurements. *Procedia Engineering*, 42:295–302, 2012.

[35] J Liu, JR Grace, and X Bi. Novel multifunctional optical-fiber probe: I. development and validation. *AIChE journal*, 49(6):1405–1420, 2003.

[36] P Bai, UJ Etim, Z Yan, S Mintova, Z Zhang, Z Zhong, and X Gao. Fluid catalytic cracking technology: current status and recent discoveries on catalyst contamination. *Catalysis Reviews*, pages 1–73, 2018.

[37] CT Crowe, JD Schwarzkopf, M Sommerfeld, , and Y Tsuji. *Multiphase flows with droplets and particles.* CRC press, Boca Raton, USA, 2011.

[38] SAJ Morsi and AJ Alexander. An investigation of particle trajectories in two-phase flow systems. *Journal of Fluid mechanics*, 55(2):193–208, 1972.

[39] D Kunii and O Levenspiel. Bubbling bed model for kinetic processes in fluidized beds. gas-solid mass and heat transfer and catalytic reactions. *Industrial & Engineering Chemistry Process Design and Development*, 7(4):481–492, 1968.

[40] TL Bergman, P Incropera, DP DeWitt, and AS Lavine. *Fundamentals of heat and mass transfer*. John Wiley & Sons, New York, USA, 2011.

[41] JA Souza, JVC Vargas, JC Ordonez, WP Martignoni, and OF von Meien. Thermodynamic optimization of fluidized catalytic cracking (fcc) units. *International Journal of Heat and Mass Transfer*, 54(5-6):1187–1197, 2011.

[42] K Ropelato, HF Meier, and MA Cremasco. Cfd study of gas–solid behavior in downer reactors: an eulerian–eulerian approach. *Powder Technology*, 154(2-3):179–184, 2005.

[43] A Lanza and H de Lasa. Scaling-up down flow reactors. cpfd simulations and model validation. *Computers & Chemical Engineering*, 101:226–242, 2017.

[44] VA Petrov and V Yu Reznik. Measurement of the emissivity of quartz glass. *High Temp.-High Pressures*, 4:687–693, 1972.

[45] S Al-Khattaf and H De Lasa. Catalytic cracking of cumene in a riser simulator: a catalyst activity decay model. *Industrial & engineering chemistry research*, 40(23):5398–5404, 2001.

[46] JS Buchanan. Reactions of model compounds over steamed zsm-5 at simulated fcc reaction conditions. *Applied catalysis*, 74(1):83–94, 1991.

[47] DK Liguras and DT Allen. Structural models for catalytic cracking. 1. model compound reactions. *Industrial & Engineering Chemistry Research*, 28(6):665–673, 1989.

[48] S Lopez-Zamora. *In-situ characterization of the reaction progress of the fluid catalytic cracking reactions by laser diagnostic techniques*. PhD thesis, Universidad Nacional de Colombia - Sede Medellín, Medellín, Colombia, 2019.

[49] N Hosseinpour, Y Mortazavi, A Bazyari, and A Khodadadi. Synergetic effects of y-zeolite and amorphous silica-alumina as main fcc catalyst components on triisopropylbenzene cracking and coke formation. *Fuel processing technology*, 90(2):171–179, 2009.

[50] N Tukur and S Al-Khattaf. Catalytic cracking of n-dodecane and alkyl benzenes over fcc zeolite catalysts: time on stream and reactant converted models. *Chemical Engineering and Processing: Process Intensification*, 44(11):1257–1268, 2005.

[51] MT Shah, RP Utikar, VK Pareek, GM Evans, and JB Joshi. Computational fluid dynamic modelling of fcc riser: a review. *chemical engineering research and design*, 111:403–448, 2016.

[52] YN Kim, C Wu, and Y Cheng. Cfd simulation of hydrodynamics of gas–solid multiphase flow in downer reactors: revisited. *Chemical engineering science*, 66(21):5357–5365, 2011.

[53] GC Lopes, LM Rosa, M Mori, JR Nunhez, and WP Martignoni. Three-dimensional modeling of fluid catalytic cracking industrial riser flow and reactions. *Computers & Chemical Engineering*, 35(11):2159–2168, 2011.

[54] ANSYS Fluent. ANSYS inc. 15.0 theory guide, 2013.

[55] Aspen Plus. Aspen plus user guide. *Aspen Technology Limited, Cambridge, USA*, 2003.

[56] VV Ranade. *Computational flow modeling for chemical reactor engineering*, volume 5. Academic Press, San Diego, USA, 2001.

[57] DF Swinehart. The beer-lambert law. *Journal of chemical education*, 39(7):333, 1962.

[58] AE Klingbeil. *Mid-IR laser absorption diagnostics for hydrocarbon vapor sensing in harsh environments*. PhD thesis, Stanford University, Stanford, USA, 2007.

[59] MF Modest. *Radiative heat transfer*. Academic press, Oxford, UK, 2013.

[60] DA Skoog, DM West, FJ Holler, and S Crouch. *Fundamentals of analytical chemistry*. Nelson Education, Belmont, USA, 2013.

[61] K Bryden, G Weatherbee, and ET Habib. Flexible pilot plant technology for evaluation of unconventional feedstocks and processes. *Catalagram*, 113:3–21, 2013.